Research group
"Control of Renewable Energy Systems"
Munich School of Engineering
Technische Universität München
Prof. Dr.-Ing. Christoph M. Hackl

Christoph Grabher

Master Thesis

Optimized Pulse Patterns to Minimize the Current Harmonic Content in the DC-link of a two-level VSI

Research group
"Control of Renewable Energy Systems"
Munich School of Engineering
Technische Universität München
Prof. Dr.-Ing. Christoph M. Hackl
Lichtenbergstr. 4a, 85748 Garching
Tel.: 089/289 52725 Fax: 089/289 52799 email: christoph.hackl@tum.de

Master Thesis Nr.: MA022

Author	:	Christoph Grabher * 03.11.1992 Mahd 75 6972 Fussach
Course of studies	:	Electrical and Computer Engineering Focus Electrical Drive Systems and Power Electronics
Title	:	Optimized Pulse Patterns to Minimize the Current Harmonic Content in the DC-link of a two-level VSI
Supervisor	:	M.Sc. Athina Birda
Begin	:	08.05.2018
End	:	30.09.2018
Final presentation	:	19.09.2018

Prof. Dr.-Ing. Christoph M. Hackl

Declaration

The presented work is based on research carried out at the research group “Control of Renewable Energy Systems“ at the Munich School of Engineering, Technische Universität München under the supervision of Prof. Dr.-Ing. Christoph M. Hackl. No part of this thesis has been submitted elsewhere for any other degree or qualification and it is all my own work unless referenced to the contrary in the text.

Christoph Grabher

Freigabe durch Dipl.-Ing. Jörg Reuß:

Jörg Reuß

Sperrvermerk
Die Arbeit beinhaltet vertrauliche Informationen, die der Geheimhaltung unterliegen. Aus diesem Grund darf die Arbeit ohne vorherige schriftliche Zustimmung der BMW Group nicht vervielfältigt oder veröffentlicht werden. Dieser Zustimmungsvorbehalt endet am 01.10.2021.

Acknowledgment

I take this opportunity to express gratitude to my thesis advisor M.Sc. Athina Birda at the BMW Group, currently PhD candidate at the Technical University of Munich. She supported and inspired me during my work, which was challenging, satisfying and very educational for me. Furthermore, I would like to thank Prof. Dr.-Ing. Christoph M. Hackl, head of the research group CRES for supervising this thesis at university level.

Christoph Grabher

Contents

List of Figures

List of Tables

Nomenclature

AC	alternating current
DC	direct current
EMC	electromagnetic compatibility
EMI	electromagnetic interferences
HWS	half wave symmetry
LUT	look-up table
OPP	optimized pulse patterns
PMSM	permanent magnet synchronous machine
PWM	pulse width modulation
QWS	quarter wave symmetry
RMS	root main square
SHEPWM	selective harmonic elimination pulse width modulation
SOPWM	synchronous pulse width modulation
SPWM	sine triangle pulse width modulation
SVPWM	space vector pulse width modulation
THD	total harmonic distortion
VSI	voltage source inverter

List of Symbols

α, β	static reference frame
$\alpha_1, \alpha_2, \alpha_3, \alpha_4$	independent switching angles
γ	additional phase shift for HWS signal forms
λ	anisotropy factor
ν	number of the harmonic order
ω	angular frequency
ω_m	mechanical angular speed
ω_r	electrical angular speed
ϕ_0	initial rotor position
ψ_{PM}	permanent magnet flux linkage
$\theta_{CH,\nu}$	phase of the equivalent network for every harmonic wave
θ_U	load voltage phase
A_{cos}	amplitude of the cosine part of $i_c(t)$
A_{sin}	amplitude of the sine part of $i_c(t)$
a_0, a_ν, b_ν	Fourier coefficients
C_{DC}	DC-link capacitor
d, q	rotating reference frame
$H_{CH,\nu}$	transfer function of the equivalent network for every harmonic wave
i_b	battery current
$i_{c,RMS}$	RMS capacitor current
i_C	DC-link current
$i_{inv,u}, i_{inv,v}, i_{inv,w}$	inverter currents caused by the according phase
$i_{inv\_cos,\nu}$	cosine part of the harmonic inverter current
$i_{inv\_sin,\nu}$	sine part of the harmonic inverter current
i_{inv}	inverter current
i_{inv_DC}	DC component of the inverter current
i_{inv_DC1}	DC inverter current caused by DC group 1
i_{inv_DC2}	DC inverter current caused by DC group 2
i_{inv_group1}	harmonic inverter current caused by harmonics group 1
i_{inv_group2}	harmonic inverter current caused by harmonics group 2
i_{inv_group3}	harmonic inverter current caused by harmonics group 3
I_{THD}	harmonic current in the output signal

i_s^d, i_s^q	stator currents in the (d,q)-coordinate system
i_s^u, i_s^v, i_s^w	stator currents of the PMSM in the (u,v,w)-coordinate system
L_1	equivalent inductance
L_i	internal inductance of the battery stack
L_l	series inductance of the connecting cable
L_s^d	stator inductance in d-direction
L_s^q	stator inductance in q-direction
m	modulation index
n_m	mechanical rotational speed
p	number of pole pairs
p_v	power dissipation produced in the capacitor
R_{ESR}	equivalent series resistor
R_1	equivalent resistance
R_i	internal resistor of the battery stack
R_l	series resistor of the connecting cable
R_s	stator resistor
S^u, S^v, S^w	phase power switch-state
T	electrical period
t	time
$\boldsymbol{T}_c$	Clarke transformation
$\boldsymbol{T}_p$	Park transformation
U_{DC}	DC-link voltage
$u_{s,1}^d$	fundamental voltage component in d-direction
$u_{s,1}^q$	fundamental voltage component in q-direction
U_0	open-circuit voltage of the battery stack
u_s^d, u_s^q	load voltage in the (d,q)-coordinate system
u_s^u, u_s^v, u_s^w	load voltages in the (u,v,w)-coordinate system

Abstract

The DC-link current ripple is responsible for the DC-link capacitor sizing. The capacitor must be able to deliver high current peaks during operation without causing a high voltage drop. In order to fulfill EMC standards, this voltage drop must be in a specific small range. Furthermore, the current ripple causes an increase of the electrolyte temperature due to undesired resistive losses in the capacitor itself. This leads to an accelerated dry-out and so resulting breakdown of the voltage source inverter (VSI). By using optimized pulse patterns (OPP), the current ripple in the DC-link can be reduced. With the OPP, presented in this thesis, a smaller and cheaper DC-link capacitor can be used while having the same DC-voltage ripple and lifespan. To achieve this, the RMS current into the capacitor in relation to the respective switching angles must be found, and set as minimization criterion in an optimization algorithm.
Simulation results at different motor operating points validate the correctness of the derived mathematical formulation of the capacitor current and the resulting optimized angles.

Chapter 1

Introduction

Due to their high efficiency, AC-fed machines are commonly used in industry applications as well as in electrical powered vehicles. In these fields of application, speed and torque variation is necessary. Thus, the machines are mainly fed by voltage source inverters (VSI). Due to their operation in switched mode the current waveform quality suffers, which leads to current harmonics in the output signal and in the DC-link of the VSI. These undesired and harmful current harmonics in the output signal cause not only torque ripple but also undesired noise and further losses in the machine. Moreover, harmonic currents in the output signal contribute to further copper losses in the machine, which account for a major portion of the machine losses [1]. Harmonics in the DC-link of the VSI are responsible for the DC-link capacitor sizing. The DC-link capacitor must be able to deliver these harmonic currents during operation, without causing a high voltage drop in the DC-link. In order to fulfill EMC standards, this voltage drop must be in a specific small range. Furthermore, the current harmonic in the DC-link causes an increase of the electrolyte temperature due to the undesired resistive losses in the capacitor itself, which leads to an accelerated dry-out and final breakdown of the VSI. On the one hand, these negative effects can be reduced by increasing the inverter switching frequency. On the other hand, this also results in increased switching losses of the power semiconductors. Both the current harmonics and the switching losses must be minimized to optimize the total efficiency of the drive system. For this reason, the Synchronous Optimal PWM (SOPWM) or also called optimized pulse patterns (OPP)[2],[3],[4],[5],[6],[7],[8],[9] was developed and extensively investigated over the last years. The main goal of SOPWM is the limitation of the inverter switching frequency without compromising on a specific optimization criterion. The inverter pulse patterns are calculated off-line for each steady state motor operating point (modulations index m, anisotropy factor λ, motor rotational speed n_m and load voltage phase θ_U) and stored in a look-up table to be available during operation. These pulse patterns fulfill a certain optimization criterion such as minimizing the torque ripple [8],[9], the total harmonic distortion current of the output signal (I_{THD}) [2],[3],[4],[5],[6],[7] or as in this thesis described, a minimal RMS current in the DC-link of the inverter($I_{c,RMS}$). With the OPP presented in this thesis a smaller and cheaper DC-link capacitor can be used while having the same DC-voltage ripple and lifespan. To achieve this the mathematical function of the RMS current into the

capacitor must be found in relation to the switching angles, and set as minimization criterion in an optimization algorithm.
Simulation results at different motor operating points validate the correctness of the derived mathematical formulation of the capacitor current and the resulting optimized angles.

Chapter 2

Fundamentals

2.1 PMSM with High Magnetic Anisotropy

Permanent Magnet Synchronous Machines (PMSMs) are widely used due to their high power density and low maintenance. Furthermore, there is an increasing focus on PMSMs when it comes to high power and high speed motor drives [10], [11]. In order to drive the machine in many different points of operation a variable voltage source with variable output frequency is necessary. The variation of the voltage fundamental waveform amplitude and output frequency are mostly realized with a two-level Voltage Source Inverter (VSI) and a specific pulse width modulation (PWM) strategy, such as Space Vector (SVPWM) [12],[13], Sine Triangle PWM (SPWM) [14],[15], Six Step Mode [1],[7],[16],[17, 168-218],[18], Selective Harmonics Elimination PWM (SHEPWM) [7],[19] or Synchronous Optimal PWM (SOPWM) [2],[3],[4],[5],[6],[7],[8],[9] .

The general voltage equations of an anisotropic PMSM are given in the (dq)-reference frame in the form of

$$\begin{pmatrix} u_s^d \\ u_s^q - \omega_r \psi_{PM} \end{pmatrix} = \begin{bmatrix} R_s + j\omega_r L_s^d & -\omega_r L_s^q \\ \omega_r L_s^d & R_s + j\omega_r L_s^q \end{bmatrix} \begin{pmatrix} i_s^d \\ i_s^q \end{pmatrix} \tag{2.1}$$

where R_S describes the stator resisto , ω_r is the electrical angular speed of the reference frame, ψ_{PM} is the permanent magnet flux linkage and L_s^d, L_s^q are the d- and q-axis inductances, respectively [2].

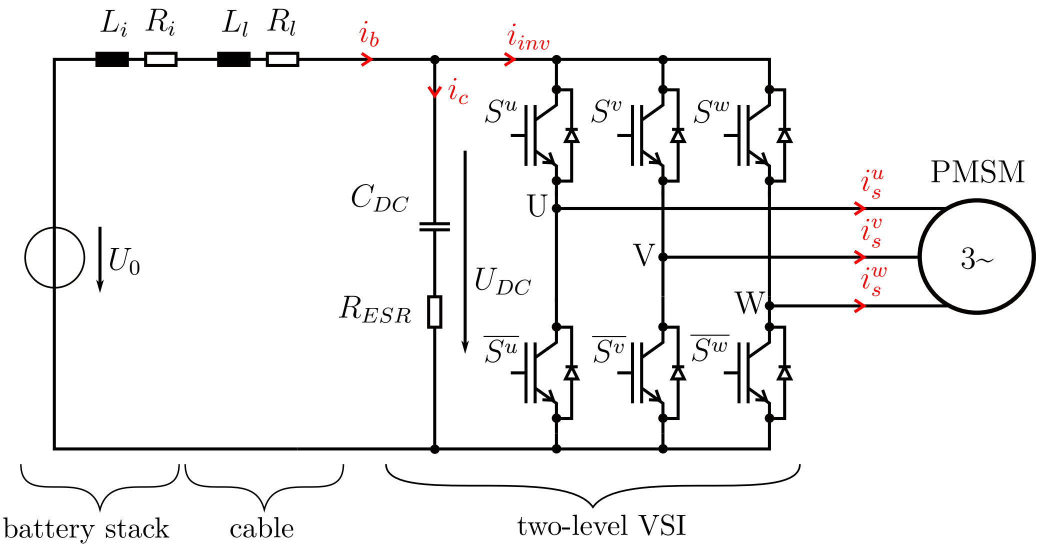

Figure 2.1: *Equivalent circuit of the battery stack, cables, VSI and PMSM*

2.2 Two-level Voltage Source Inverter

Two-level VSI are commonly used because of their low complexity, low-cost and robustness. But they do have some disadvantages. The peak current stress for the capacitor C_{DC} is immense, which leads to a DC-voltage ripple. If the capacitor value is too low the DC-link voltage drops for high amplitudes of current harmonics. This resulting voltage ripple emits electromagnetic interferences (EMI). Another disadvantage is the resulting load current ripple due to the voltage ripple, which leads to a high THD of the load current. These disadvantages can be eliminated by more complex multilevel inverter topologies.

Figure 2.1 represents the equivalent circuit of the investigated case. U_0 is the open-circuit voltage of the battery-stack, L_i is the internal battery inductance and R_i is the battery internal resistance [20]. Effects like charge transfer or diffusion find no consideration in the battery equivalent circuit, due to their high time constant compared to the switching frequency of the power-semiconductors, which is several decimal powers higher. Further L_l and R_l describe the inductance and the resistance of the connecting cable. C_{DC} is the DC-link capacitor and R_{ESB} represents the equivalent serial resistance of the capacitor. S^u, S^v, S^w and $\overline{S^u}$, $\overline{S^v}$, $\overline{S^w}$ are the switching states of the power-modules (IGBTs). For the further consideration the inductances L_i and L_l as well as the resistances R_i and R_l are combined into one inductance L_1 and one resistance R_1.

For the simulation in chapter 7 the ψ_{PM} is set to $0.033\frac{\text{Vs}}{\text{A}}$, $C_{DC} = 360\text{µF}$, $U_0 = 400\text{V}$, $R_{ESR} = 0.001\Omega$ and the stator resistor of the PMSM is defined to 0.005Ω. Furthermore, the equivalent resistor R_1 is 0.1Ω and the equivalent inductance L_1 is 2.4µH. The d- and q-axis inductances are $L_s^d = 91.95\text{µH}$ and $L_s^q = 294.24\text{µH}$, respectively.

2.3 Fourier Theory

Periodical functions and signals can be expressed as a superposition of harmonic oscillations. The frequencies of the harmonic oscillations must be integer multiples of the fundamental frequency from the periodic signal. The Fourier series is a way to sum up the simple oscillating functions, namely sine and cosine. The coefficients of this sum give a line spectrum which shows from which frequency components the time signal is composed [21, p.163-193].
A non-sinusoidal function $f(t)$ with the periodic time $T = \frac{2\pi}{\omega}$ can be separated into its harmonic components using

$$f(t) = \frac{a_0}{2} + \sum_{\nu=1}^{+\infty} [a_\nu \cos(\nu\omega t) + b_\nu \sin(\nu\omega t)], \tag{2.2}$$

where a_0, a_ν and b_ν represent the Fourier coefficients. Theses coefficients can be calculated with the following integral equations:

$$a_0 = \frac{2}{T} \int_{(T)} f(t)dt \tag{2.3}$$

$$a_\nu = \frac{2}{T} \int_{(T)} f(t) \cos(\nu\omega t)dt \tag{2.4}$$

$$b_\nu = \frac{2}{T} \int_{(T)} f(t) \sin(\nu\omega t)dt \tag{2.5}$$

The type of convergence depends on the smoothness of the function $f(t)$. It is essential for absolute convergence that the Fourier coefficients form absolutely convergent series, and the function in the period interval satisfies the Dirichlet conditions. The Fourier series converge very slowly for discontinuous functions like a PWM signal. In the discontinuous transition the Fourier series converge to the arithmetic average of the left side and right side function limit.
Near the discontinuous transitions, overshoots occur in the plotted Fourier series. This effect is called Gibbs phenomenon [21, p.163-193].

2.4 Waveform Definition and Properties

The half wave symmetric (HWS) PWM voltage, which can be measured between the terminal U and the virtual mid-point of the DC-bus, is defined by the four independent switching angles α_1-α_4 and the voltage amplitude $\pm\frac{U_{DC}}{2}$.
Figure 2.3 shows the differences between half wave symmetric (HWS) and quarter wave symmetric (QWS) voltage signals. By using HWS there are two times more independent switching angles which will help at the end of this theses, where an optimization of the RMS current in the DC-link capacitor is executed, because so the optimization algorithm has more degrees of freedom for minimizing the RMS current. A disadvantage is the resulting phase shift of the fundamental voltage by using HWS switching angles. This phase shift must be taken into account during calculation. The load voltage can be measured between terminal U and the mid-point of the star-connected motor (see figure 2.1).

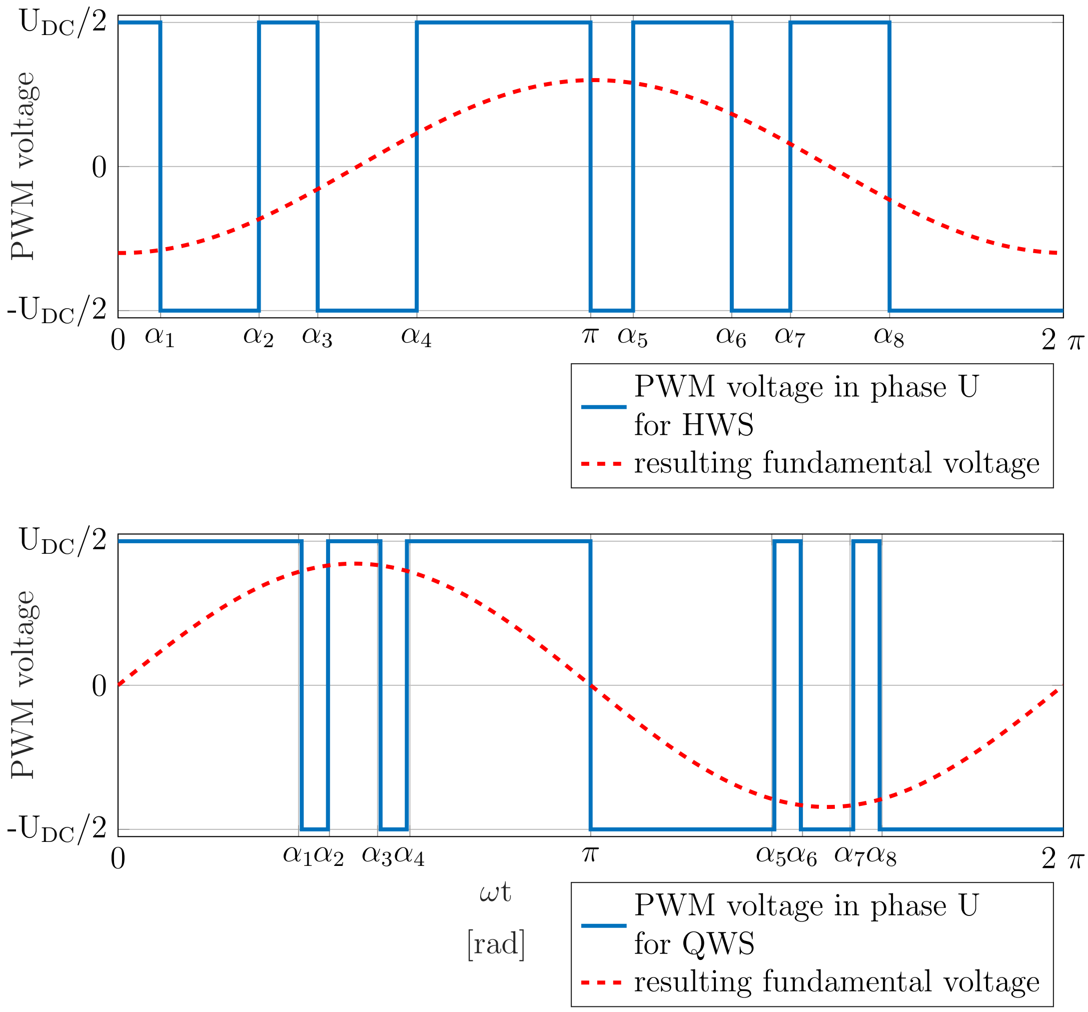

Figure 2.2: *Difference between HWS- and QWS-signals with four switching angles.*

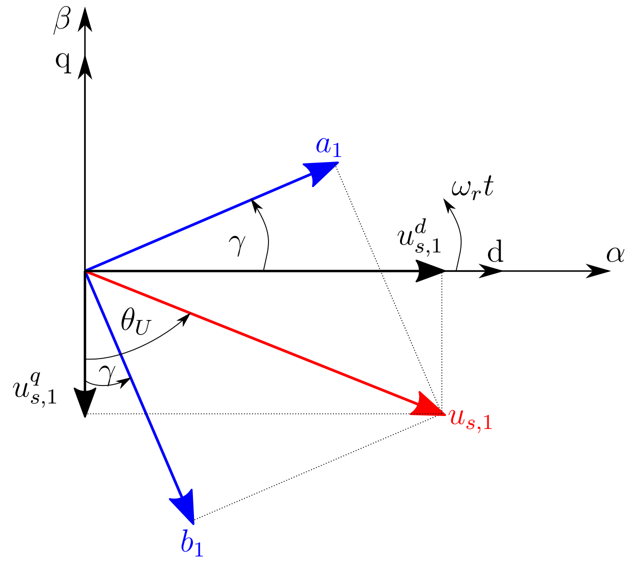

Figure 2.3: *Resulting fundamental voltage vector in the (d,q)-reference frame with the angles γ and θ_U*

Figure 2.3 represents the fundamental load voltage vector. This vector and the (d,q)-reference frame rotate with the electrical angular frequency ω_r in the (α,β)-reference frame. The amplitude of this fundamental voltage vector is defined by

$$|u_{s,1}| := \sqrt{(u^q_{s,1})^2 + (u^d_{s,1})^2}, \tag{2.6}$$

where $u^d_{s,1}$ and $u^q_{s,1}$ are the voltage components in the orthogonal (d,q)-reference frame.
Further, the amplitude of the fundamental load voltage vector indicates the modulation index m, which is defined by

$$|u_{s,1}| := m\frac{U_{DC}}{2}, \tag{2.7}$$

where U_{DC} is the DC-link voltage.
The angle γ represents the resulting phase shift caused by the vector a_1 and b_1 which indicates an unsymmetrical arrangement of the switching angles in a half wave of the electrical period. This leads to a further shift in the phase of the load voltage fundamental θ_U. For quarter-wave symmetric (QWS) switching patterns the a_ν Fourier component gets zero and so γ gets zero too. In this thesis half-wave symmetric (HWS) switching patterns are used with four independent switching angles (α_1,α_2, α_3 and α_4) over a half electrical period.
The resulting angle of the load voltage is defined as

$$\theta_U := \arctan(\frac{u^d_{s,1}}{u^q_{s,1}}). \tag{2.8}$$

For three-phase star-connected motors this load voltage for phase U can be expressed by

$$u_s^u(t) = \sum_{\nu=1,5,7,11,13...}^{+\infty} [a_\nu \cos(\nu(\omega_r t + \gamma)) + b_\nu \sin(\nu(\omega_r t + \gamma))], \tag{2.9}$$

where a_ν and b_ν are the Fourier components and ν describes the order of the harmonic. It is worth mentioning that load voltage harmonics with the order multiple of 3 are zero due to the star-connection of the motor windings.

2.5 Synchronous Optimal Pulse Width Modulation

Synchronous Optimal PWM (SOPWM) or the methode of Optimized Pulse Patterns (OPP) describes a PWM strategy for low switching frequencies and low dynamic applications, like in automotive applications, since the changes of the load torque and motor speed are rather slow[2]. In the 1970s the concept of SOPWM was commonly used because the available power semiconductors were relatively slow and not able to obtain a high enough switching frequency to reduce the current harmonics for dynamic and fast rotating applications. Nowadays, the power-semiconductors are able to operate at very high switching frequencies but this leads to higher switching losses. To improve the overall drive efficiency, motor and switching losses need to be considered. The main goal of SOPWM is the limitation of the inverter switching frequency, without compromising on the quality of the optimization criterion, in the most cases the inverter output current waveform. This is of most importance, because the current harmonics are responsible for further coper losses in the machine and those account for a major portion of the machine losses. The inverter pulse patterns are calculated off-line for each steady state motor operating point (modulations index m, anisotropy factor $\lambda = \frac{L_s^q}{L_s^d}$ and load angle θ_U) and stored in a look-up table to be available during operation. These pulse patterns fulfill a certain optimization criterion like minimizing the torque ripple, speed ripple, the total harmonic distortion current (I_{THD})[2] or as in this thesis described a minimized RMS current into the DC-link capacitor of the inverter. Last but not least, the battery-stack voltage can be fully exploited. Due to fewer switching-operations, the fundamental voltage amplitude rises. This leads to an increased motor rated speed as well as output power.

In addition to the already mentioned disadvantage of the low dynamics of SOPWM, there are further disadvantages, such as the computing time for the optimal switching angles, where discontinuous switching angles most likely occur. These discontinuous switching angles pose enormous problems for the current control loop. To reduce this effect the switching angles get smoothed and then stored in the look-up table. Adapting the optimal switching angles to get continuous patterns means not using the full potential of SOPWM. Furthermore, for small modulation indices SOPWM hardly has any benefits compared to Space Vector PWM (SVPWM). So a combination of SVPWM and SOPWM is necessary to use the full range of the operating points efficiently [3].

Another PWM strategy for low switching frequencies is the Selective Harmonic

Elimination PWM (SHEPWM) [7],[19]. However, it was found that elimination of the lower order harmonics not always leads to optimal motor performance. The conclusion was that it is better to use degrees of freedom for minimization of overall harmonics than complete elimination of certain lower order harmonics [7]. Thus, optimal PWM methods have been developed to minimize the overall effects of harmonics [2],[3],[4],[7].

Chapter 3

Derivation of the Output Phase Current of the VSI

This chapter concludes the information given by my supervisor's paper [2] (Athina Birda), currently PhD candidate at the Technical University of Munich.

3.1 Simplifications

In the following chapter and in the further thesis the stator resistance of the PMSM find no further consideration and is set to zero. For the calculation of the phase currents (i_s^u,i_s^v,i_s^w) the DC-link voltage U_{DC} is set constantly to 400 Volts.

3.2 Formulation of the Load Voltage in Relation to the Switching Angles

For three-phase star-connected motors, the load voltage in Fourier series notation with respect to the half wave symmetric (HWS) switching signal angles are given by

$$\boldsymbol{u}_s^{uvw}(t) = \begin{pmatrix} u_s^u(t) \\ u_s^v(t) \\ u_s^w(t) \end{pmatrix} = \begin{pmatrix} U_{DC} \sum\limits_{\nu=1,5,7\ldots}^{+\infty} [b_\nu \sin(\nu(\omega t + \gamma)) + a_\nu \cos(\nu(\omega t + \gamma))] \\ U_{DC} \sum\limits_{\nu=1,5,7\ldots}^{+\infty} [b_\nu \sin(\nu(\omega t + \gamma - \frac{2\pi}{3})) + a_\nu \cos(\nu(\omega t + \gamma - \frac{2\pi}{3}))] \\ U_{DC} \sum\limits_{\nu=1,5,7\ldots}^{+\infty} [b_\nu \sin(\nu(\omega t + \gamma - \frac{4\pi}{3})) + a_\nu \cos(\nu(\omega t + \gamma - \frac{4\pi}{3}))] \end{pmatrix}, \tag{3.1}$$

where the Fourier coefficients a_ν and b_ν generally are

$$\begin{aligned} a_\nu &= \frac{1}{\pi} \int_0^{2\pi} f(\omega t) \cos(\nu \omega t) \\ &= \frac{1}{\pi\nu}(1 - \cos(\nu\alpha_1) + \cos(\nu\alpha_2) - \cos(\nu\alpha_3) + \cos(\nu\alpha_4) - \cos(\nu\pi) \\ &+ \cos(\nu(\pi + \alpha_1)) - \cos(\nu(\pi + \alpha_2)) + \cos(\nu(\pi + \alpha_3)) - \cos(\nu(\pi + \alpha_4))) \end{aligned} \tag{3.2}$$

$$\begin{aligned} b_\nu &= \frac{1}{\pi}\int_0^{2\pi} f(\omega t)\sin(\nu\omega t) \\ &= \frac{1}{\pi\nu}(\sin(\nu\alpha_1) - \sin(\nu\alpha_2) + \sin(\nu\alpha_3) - \sin(\nu\alpha_4) + \sin(\nu\pi) \\ &- \sin(\nu(\pi+\alpha_1)) + \sin(\nu(\pi+\alpha_2)) - \sin(\nu(\pi+\alpha_3)) + \sin(\nu(\pi+\alpha_4))). \end{aligned} \tag{3.3}$$

For odd order non triple harmonics the Fourier coefficients become simplified to

$$a_\nu = \frac{2}{\nu\pi}(1 - \cos(\nu\alpha_1) + \cos(\nu\alpha_2) - \cos(\nu\alpha_3) + \cos(\nu\alpha_4)) \tag{3.4}$$

and

$$b_\nu = \frac{2}{\nu\pi}(\sin(\nu\alpha_1) - \sin(\nu\alpha_2) + \sin(\nu\alpha_3) - \sin(\nu\alpha_4)). \tag{3.5}$$

The phase voltages in the three-phase system can be transformed into the synchronous rotating (d,q)-coordinate system using the Clarke-Park transformation.

$$\boldsymbol{T}_c = \frac{2}{3}\begin{bmatrix} 1 & -\frac{1}{2} & -\frac{1}{2} \\ 0 & \frac{\sqrt{3}}{2} & -\frac{\sqrt{3}}{2} \end{bmatrix} \tag{3.6}$$

$$\boldsymbol{T}_p(\omega_r t + \phi_0) = \begin{bmatrix} \cos(\omega_r t + \phi_0) & -\sin(\omega_r t + \phi_0) \\ \sin(\omega_r t + \phi_0) & \cos(\omega_r t + \phi_0) \end{bmatrix} \tag{3.7}$$

$$\boldsymbol{u}_s^{dq}(t) = \boldsymbol{T}_p^{-}1(\omega_r t\phi_0)\boldsymbol{T}_c\boldsymbol{u}_s^{uvw} \tag{3.8}$$

$$\begin{aligned} &\boldsymbol{u}_s^{dq}(t) = \\ &= U_{DC}\begin{pmatrix} a_1\cos(\gamma) & b_1\sin(\gamma) \\ a_1\sin(\gamma) & -b_1\cos(\gamma) \end{pmatrix} \\ &+ U_{DC}\begin{pmatrix} \sum\limits_{\nu=6i}^{+\infty}[a_{\nu-1}\cos(\nu(\omega_r t + \phi_0) + (\nu-1)\gamma) + a_{\nu+1}\cos(\nu(\omega_r t + \phi_0) + (\nu+1)\gamma)] \\ \sum\limits_{\nu=6i}^{+\infty}[-a_{\nu-1}\sin(\nu(\omega_r t + \phi_0) + (\nu-1)\gamma) + a_{\nu+1}\sin(\nu(\omega_r t + \phi_0) + (\nu+1)\gamma)] \end{pmatrix} \\ &+ U_{DC}\begin{pmatrix} \sum\limits_{\nu=6i}^{+\infty}[b_{\nu-1}\sin(\nu(\omega_r t + \phi_0) + (\nu-1)\gamma) + b_{\nu+1}\sin(\nu(\omega_r t + \phi_0) + (\nu+1)\gamma)] \\ \sum\limits_{\nu=6i}^{+\infty}[b_{\nu-1}\cos(\nu(\omega_r t + \phi_0) + (\nu-1)\gamma) - b_{\nu+1}\cos(\nu(\omega_r t + \phi_0) + (\nu+1)\gamma)] \end{pmatrix} \end{aligned} \tag{3.9}$$

It is worth mentioning that the two orthogonal voltage components in the (d,q)-reference frame contain harmonic components of multiples of six, while the load voltages in the (u,v,w)-reference frame contain $6i \pm 1$ multiples of harmonics.

Solving equation (2.1) for the currents i_s^d and i_s^q plus re-transforming the currents from the $(d{,}q)$-reference frame into the $(u{,}v{,}w)$-reference frame by applying the inverse Clarke-Park transformation (3.10) the motor phase currents (3.11),(3.12) and (3.13) can be found in relation of the switching angles.
The stator currents in vector notation in the $(u{,}v{,}w)$-reference frame are represented by

$$\begin{pmatrix} i_s^u(t) \\ i_s^v(t) \\ i_s^w(t) \end{pmatrix} = \boldsymbol{T}_c^{-1}\boldsymbol{T}_p(\omega_r t + \phi_0)\begin{pmatrix} i_s^d(t) \\ i_s^q(t) \end{pmatrix}. \tag{3.10}$$

In detail

$$\begin{aligned} i_s^u(t) = {} & U_{DC}\frac{u_{s,0}^d + \omega_r L_s^q(u_{s,0}^q - (\omega_r\psi_{pm}))}{\omega_r^2 L_s^d L_s^q}\cos(\omega_r t) \\ & + U_{DC}\frac{u_{s,0}^d}{\omega_r L_s^q}\sin(\omega_r t) + \frac{U_{DC}}{2\omega_r L_s^q}\sum_{\nu=6i}^{+\infty}\Bigg[\\ & \left(\frac{a_{\nu+1}}{\nu+1}(\lambda-1)\cos(2\gamma) + \frac{a_{\nu-1}}{\nu-1}(\lambda+1)\right. \\ & \left. + \frac{b_{\nu+1}}{\nu+1}(\lambda-1)\sin(2\gamma)\right)\sin((\nu-1)(\omega_r t+\gamma)) \\ & + \left(\frac{a_{\nu+1}}{\nu+1}(\lambda-1)\sin(2\gamma) - \frac{b_{\nu-1}}{\nu-1}(\lambda+1)\right. \\ & \left. - \frac{b_{\nu+1}}{\nu+1}(\lambda-1)\cos(2\gamma)\right)\cos((\nu-1)(\omega_r t+\gamma)) \\ & + \left(\frac{a_{\nu-1}}{\nu-1}(\lambda-1)\cos(2\gamma) + \frac{a_{\nu+1}}{\nu+1}(\lambda+1)\right. \\ & \left. - \frac{b_{\nu-1}}{\nu-1}(\lambda-1)\sin(2\gamma)\right)\sin((\nu+1)(\omega_r t+\gamma)) \\ & + \left(-\frac{a_{\nu-1}}{\nu-1}(\lambda-1)\sin(2\gamma) - \frac{b_{\nu+1}}{\nu+1}(\lambda+1)\right. \\ & \left. - \frac{b_{\nu-1}}{\nu-1}(\lambda-1)\cos(2\gamma)\right)\cos((\nu+1)(\omega_r t+\gamma))\Bigg], \end{aligned} \tag{3.11}$$

$$
\begin{aligned}
i_s^v(t) = {} & U_{DC}\frac{u_{s,0}^d + \omega_r L_s^q(u_{s,0}^q - (\omega_r\psi_{pm}))}{\omega_r^2 L_s^d L_s^q}\cos(\omega_r t - \frac{2\pi}{3}) \\
& + U_{DC}\frac{u_{s,0}^d}{\omega_r L_s^q}\sin(\omega_r t - \frac{2\pi}{3}) + \frac{U_{DC}}{2\omega_r L_s^q}\sum_{\nu=6i}^{+\infty}\Bigg[\\
& \Bigg(\frac{a_{\nu+1}}{\nu+1}(\lambda-1)\cos(2\gamma) + \frac{a_{\nu-1}}{\nu-1}(\lambda+1) \\
& + \frac{b_{\nu+1}}{\nu+1}(\lambda-1)\sin(2\gamma)\Bigg)\sin((\nu-1)(\omega_r t + \gamma - \frac{2\pi}{3})) \\
& + \Bigg(\frac{a_{\nu+1}}{\nu+1}(\lambda-1)\sin(2\gamma) - \frac{b_{\nu-1}}{\nu-1}(\lambda+1) \\
& - \frac{b_{\nu+1}}{\nu+1}(\lambda-1)\cos(2\gamma)\Bigg)\cos((\nu-1)(\omega_r t + \gamma - \frac{2\pi}{3})) \\
& + \Bigg(\frac{a_{\nu-1}}{\nu-1}(\lambda-1)\cos(2\gamma) + \frac{a_{\nu+1}}{\nu+1}(\lambda+1) \\
& - \frac{b_{\nu-1}}{\nu-1}(\lambda-1)\sin(2\gamma)\Bigg)\sin((\nu+1)(\omega_r t + \gamma - \frac{2\pi}{3})) \\
& + \Bigg(-\frac{a_{\nu-1}}{\nu-1}(\lambda-1)\sin(2\gamma) - \frac{b_{\nu+1}}{\nu+1}(\lambda+1) \\
& - \frac{b_{\nu-1}}{\nu-1}(\lambda-1)\cos(2\gamma)\Bigg)\cos((\nu+1)(\omega_r t + \gamma - \frac{2\pi}{3}))\Bigg]
\end{aligned}
\tag{3.12}
$$

and

$$
\begin{aligned}
i_s^w(t) = {} & U_{DC}\frac{u_{s,0}^d + \omega_r L_s^q(u_{s,0}^q - (\omega_r\psi_{pm}))}{\omega_r^2 L_s^d L_s^q}\cos(\omega_r t - \frac{4\pi}{3}) \\
& + U_{DC}\frac{u_{s,0}^d}{\omega_r L_s^q}\sin(\omega_r t - \frac{4\pi}{3}) + \frac{U_{DC}}{2\omega_r L_s^q}\sum_{\nu=6i}^{+\infty}\Bigg[\\
& \Bigg(\frac{a_{\nu+1}}{\nu+1}(\lambda-1)\cos(2\gamma) + \frac{a_{\nu-1}}{\nu-1}(\lambda+1) \\
& + \frac{b_{\nu+1}}{\nu+1}(\lambda-1)\sin(2\gamma)\Bigg)\sin((\nu-1)(\omega_r t + \gamma - \frac{4\pi}{3})) \\
& + \Bigg(\frac{a_{\nu+1}}{\nu+1}(\lambda-1)\sin(2\gamma) - \frac{b_{\nu-1}}{\nu-1}(\lambda+1) \\
& - \frac{b_{\nu+1}}{\nu+1}(\lambda-1)\cos(2\gamma)\Bigg)\cos((\nu-1)(\omega_r t + \gamma - \frac{4\pi}{3})) \\
& + \Bigg(\frac{a_{\nu-1}}{\nu-1}(\lambda-1)\cos(2\gamma) + \frac{a_{\nu+1}}{\nu+1}(\lambda+1) \\
& - \frac{b_{\nu-1}}{\nu-1}(\lambda-1)\sin(2\gamma)\Bigg)\sin((\nu+1)(\omega_r t + \gamma - \frac{4\pi}{3})) \\
& + \Bigg(-\frac{a_{\nu-1}}{\nu-1}(\lambda-1)\sin(2\gamma) - \frac{b_{\nu+1}}{\nu+1}(\lambda+1) \\
& - \frac{b_{\nu-1}}{\nu-1}(\lambda-1)\cos(2\gamma)\Bigg)\cos((\nu+1)(\omega_r t + \gamma - \frac{4\pi}{3}))\Bigg],
\end{aligned}
\tag{3.13}
$$

where the anisotropic factor $\lambda = \frac{L_s^q}{L_s^d}$.

Chapter 4

Derivation of the Inverter Current of the VSI

The digital switching signals for the power-semiconductor are not steady functions and difficult to handle. By decomposing these not steady functions into steady sine and cosine functions by using the Fourier theory these functions become manageable. The motor phase currents where derived in the previous chapter 3 in dependence of the DC-link voltage and the switching angles. For this thesis, four independent switching angles with a HWS constellation are used. The resulting inverter current i_{inv} is the sum of the motor phase currents in the active inverter legs. This means that the Fourier series of the digital switching signals for the power-semiconductor must be multiplied with the Fourier series of the motor phase currents from chapter 3 for all three phases and summed up at the end.

The Fourier series of the switching states can be expressed by [22]

$$\begin{aligned}
S^u(t) &= \frac{a_0}{2} + \sum_{\nu=2i-1}^{+\infty} [b_\nu \sin(\nu\omega t) + a_\nu \cos(\nu\omega t)] \\
S^v(t) &= \frac{a_0}{2} + \sum_{\nu=2i-1}^{+\infty} [b_\nu \sin(\nu(\omega t - \frac{2\pi}{3})) + a_\nu \cos(\nu(\omega t - \frac{2\pi}{3}))] \\
S^w(t) &= \frac{a_0}{2} + \sum_{\nu=2i-1}^{+\infty} [b_\nu \sin(\nu(\omega t - \frac{4\pi}{3})) + a_{s\nu} \cos(\nu(\omega t - \frac{4\pi}{3}))],
\end{aligned} \tag{4.1}$$

where the Fourier coefficients for each individual harmonic signal are

$$\begin{aligned}
a_0 &= \frac{1}{\pi} \int_0^{2\pi} f(\omega t) d\omega t \\
&= \frac{1}{\pi}(\alpha_1 + \alpha_3 - \alpha_2 + \pi - \alpha_4 + \pi + \alpha_2 - \pi - \alpha_1 + \pi + \alpha_4 - \pi - \alpha_3) \\
&= \frac{\pi}{\pi} = 1
\end{aligned} \tag{4.2}$$

$$
\begin{aligned}
a_\nu &= \frac{1}{\pi}\int_0^{2\pi} f(\omega t)\cos(\nu\omega t) \\
&= \frac{1}{\pi\nu}(1-\cos(\nu\alpha_1)+\cos(\nu\alpha_2)-\cos(\nu\alpha_3)+\cos(\nu\alpha_4)-\cos(\nu\pi) \\
&+\cos(\nu(\pi+\alpha_1))-\cos(\nu(\pi+\alpha_2))+\cos(\nu(\pi+\alpha_3))-\cos(\nu(\pi+\alpha_4)))
\end{aligned} \tag{4.3}
$$

$$
\begin{aligned}
b_\nu &= \frac{1}{\pi}\int_0^{2\pi} f(\omega t)\sin(\nu\omega t) \\
&= \frac{1}{\pi\nu}(\sin(\nu\alpha_1)-\sin(\nu\alpha_2)+\sin(\nu\alpha_3)-\sin(\nu\alpha_4)+\sin(\nu\pi) \\
&-\sin(\nu(\pi+\alpha_1))+\sin(\nu(\pi+\alpha_2))-\sin(\nu(\pi+\alpha_3))+\sin(\nu(\pi+\alpha_4))).
\end{aligned} \tag{4.4}
$$

For odd order harmonics the Fourier coefficients become simplified to

$$
a_\nu = \frac{2}{\nu\pi}(1-\cos(\nu\alpha_1)+\cos(\nu\alpha_2)-\cos(\nu\alpha_3)+\cos(\nu\alpha_4)) \tag{4.5}
$$

and

$$
b_\nu = \frac{2}{\nu\pi}(\sin(\nu\alpha_1)-\sin(\nu\alpha_2)+\sin(\nu\alpha_3)-\sin(\nu\alpha_4)). \tag{4.6}
$$

The inverter current with respect to the switching angles can be calculated by applying Kirchhoff's law. The current in the DC-link is the sum of the phase currents in all active inverter legs.

$$
\begin{aligned}
i_{inv}(t) &= i_{inv,u}(t)+i_{inv,v}(t)+i_{inv,w}(t) \\
&= S^u(t)i_s^u(t)+S^v(t)i_s^v(t)+S^w(t)i_s^w(t)
\end{aligned} \tag{4.7}
$$

Equation (4.7) represents the inverter current in relation to the switching angles assuming that the stator resistance is small and, thus, negligible. A further simplification is made, that the DC-link voltage remains constant, during operation. The resulting failure of the inverter current for other operating points (see chapter 7) is approximately 1-3 % and can be ignored without hesitation. The variation of the DC-link voltage during operation is primary caused by the new considered resistor R_1 and inductance L_1. The small impact on the overall accuracy is proven with an equivalent simulation model of the PMSM, battery stack and VSI in Simulink combined with PLECS (see figure 7.5).

The inverter current for phase U is calculated by

$$
\begin{aligned}
&i_{inv,u}(t) = S^u(t) i_s^u(t)\\
=&\Big[S_0^u(t) + S_1^u(t) + S_3^u(t) + S_5^u(t) + S_7^u(t) + S_9^u(t) + S_{11}^u(t) + ...\Big]\\
&\Big[i_{s,1}^u(t) + i_{s,5}^u(t) + i_{s,7}^u(t) + i_{s,11}^u(t) + i_{s,13}^u(t) + ...\Big]\\
=&S_0^u(t)i_{s,1}^u(t) + S_0^u(t)i_{s,5}^u(t) + S_0^u(t)i_{s,7}^u(t) + S_0^u(t)i_{s,11}^u(t) + S_0^u(t)i_{s,13}^u(t) + ...\\
&+ S_1^u(t)i_{s,1}^u(t) + S_1^u(t)i_{s,5}^u(t) + S_1^u(t)i_{s,7}^u(t) + S_1^u(t)i_{s,11}^u(t) + S_1^u(t)i_{s,13}^u(t) + ...\\
&+ S_3^u(t)i_{s,1}^u(t) + S_3^u(t)i_{s,5}^u(t) + S_3^u(t)i_{s,7}^u(t) + S_3^u(t)i_{s,11}^u(t) + S_3^u(t)i_{s,13}^u(t) + ...\\
&+ S_5^u(t)i_{s,1}^u(t) + S_5^u(t)i_{s,5}^u(t) + S_5^u(t)i_{s,7}^u(t) + S_5^u(t)i_{s,11}^u(t) + S_5^u(t)i_{s,13}^u(t) + ...\\
&+ S_7^u(t)i_{s,1}^u(t) + S_7^u(t)i_{s,5}^u(t) + S_7^u(t)i_{s,7}^u(t) + S_7^u(t)i_{s,11}^u(t) + S_7^u(t)i_{s,13}^u(t) + ...\\
&+ S_9^u(t)i_{s,1}^u(t) + S_9^u(t)i_{s,5}^u(t) + S_9^u(t)i_{s,7}^u(t) + S_9^u(t)i_{s,11}^u(t) + S_9^u(t)i_{s,13}^u(t) + ...\\
&+ S_{11}^u(t)i_{s,1}^u(t) + S_{11}^u(t)i_{s,5}^u(t) + S_{11}^u(t)i_{s,7}^u(t) + S_{11}^u(t)i_{s,11}^u(t) + S_{11}^u(t)i_{s,13}^u(t) + ...\\
&+ ...
\end{aligned}
\tag{4.8}
$$

Doing the same for phase V leads to

$$
\begin{aligned}
&i_{inv,v}(t) = S^v(t) i_s^v(t)\\
=&\Big[S_0^v(t) + S_1^v(t) + S_3^v(t) + S_5^v(t) + S_7^v(t) + S_9^v(t) + S_{11}^v(t) + ...\Big]\\
&\Big[i_{s,1}^v(t) + i_{s,5}^v(t) + i_{s,7}^v(t) + i_{s,11}^v(t) + i_{s,13}^v(t) + ...\Big]\\
=&S_0^v(t)i_{s,1}^v(t) + S_0^v(t)i_{s,5}^v(t) + S_0^v(t)i_{s,7}^v(t) + S_0^v(t)i_{s,11}^v(t) + S_0^v(t)i_{s,13}^v(t) + ...\\
&+ S_1^v(t)i_{s,1}^v(t) + S_1^v(t)i_{s,5}^v(t) + S_1^v(t)i_{s,7}^v(t) + S_1^v(t)i_{s,11}^v(t) + S_1^v(t)i_{s,13}^v(t) + ...\\
&+ S_3^v(t)i_{s,1}^v(t) + S_3^v(t)i_{s,5}^v(t) + S_3^v(t)i_{s,7}^v(t) + S_3^v(t)i_{s,11}^v(t) + S_3^v(t)i_{s,13}^v(t) + ...\\
&+ S_5^v(t)i_{s,1}^v(t) + S_5^v(t)i_{s,5}^v(t) + S_5^v(t)i_{s,7}^v(t) + S_5^v(t)i_{s,11}^v(t) + S_5^v(t)i_{s,13}^v(t) + ...\\
&+ S_7^v(t)i_{s,1}^v(t) + S_7^v(t)i_{s,5}^v(t) + S_7^v(t)i_{s,7}^v(t) + S_7^v(t)i_{s,11}^v(t) + S_7^v(t)i_{s,13}^v(t) + ...\\
&+ S_9^v(t)i_{s,1}^v(t) + S_9^v(t)i_{s,5}^v(t) + S_9^v(t)i_{s,7}^v(t) + S_9^v(t)i_{s,11}^v(t) + S_9^v(t)i_{s,13}^v(t) + ...\\
&+ S_{11}^v(t)i_{s,1}^v(t) + S_{11}^v(t)i_{s,5}^v(t) + S_{11}^v(t)i_{s,7}^v(t) + S_{11}^v(t)i_{s,11}^v(t) + S_{11}^v(t)i_{s,13}^v(t) + ...\\
&+ ...
\end{aligned}
\tag{4.9}
$$

and for phase W, respectively.

$$
\begin{aligned}
&i_{inv,w}(t) = S^w(t) i_s^w(t)\\
=&\Big[S_0^w(t) + S_1^w(t) + S_3^w(t) + S_5^w(t) + S_7^w(t) + S_9^w(t) + S_{11}^w(t) + ...\Big]\\
&\Big[i_{s,1}^w(t) + i_{s,5}^w(t) + i_{s,7}^w(t) + i_{s,11}^w(t) + i_{s,13}^w(t) + ...\Big]\\
=&S_0^w(t)i_{s,1}^w(t) + S_0^w(t)i_{s,5}^w(t) + S_0^w(t)i_{s,7}^w(t) + S_0^w(t)i_{s,11}^w(t) + S_0^w(t)i_{s,13}^w(t) + ...\\
&+ S_1^w(t)i_{s,1}^w(t) + S_1^w(t)i_{s,5}^w(t) + S_1^w(t)i_{s,7}^w(t) + S_1^w(t)i_{s,11}^w(t) + S_1^w(t)i_{s,13}^w(t) + ...\\
&+ S_3^w(t)i_{s,1}^w(t) + S_3^w(t)i_{s,5}^w(t) + S_3^w(t)i_{s,7}^w(t) + S_3^w(t)i_{s,11}^w(t) + S_3^w(t)i_{s,13}^w(t) + ...\\
&+ S_5^w(t)i_{s,1}^w(t) + S_5^w(t)i_{s,5}^w(t) + S_5^w(t)i_{s,7}^w(t) + S_5^w(t)i_{s,11}^w(t) + S_5^w(t)i_{s,13}^w(t) + ...\\
&+ S_7^w(t)i_{s,1}^w(t) + S_7^w(t)i_{s,5}^w(t) + S_7^w(t)i_{s,7}^w(t) + S_7^w(t)i_{s,11}^w(t) + S_7^w(t)i_{s,13}^w(t) + ...\\
&+ S_9^w(t)i_{s,1}^w(t) + S_9^w(t)i_{s,5}^w(t) + S_9^w(t)i_{s,7}^w(t) + S_9^w(t)i_{s,11}^w(t) + S_9^w(t)i_{s,13}^w(t) + ...\\
&+ S_{11}^w(t)i_{s,1}^w(t) + S_{11}^w(t)i_{s,5}^w(t) + S_{11}^w(t)i_{s,7}^w(t) + S_{11}^w(t)i_{s,11}^w(t) + S_{11}^w(t)i_{s,13}^w(t) + ...\\
&+ ...
\end{aligned}
\tag{4.10}
$$

Rearranging the equation with the same harmonic components leads to

$$
\begin{aligned}
i_{inv}(t) = & \Big[S_0^u(t)i_{s,1}^u(t) + S_0^v(t)i_{s,1}^v(t) + S_0^w(t)i_{s,1}^w(t)\Big] + \Big[S_0^u(t)i_{s,5}^u(t) + S_0^v(t)i_{s,5}^v(t) \\
& + S_0^w(t)i_{s,5}^w(t)\Big] + \Big[S_0^u(t)i_{s,7}^u(t) + S_0^v(t)i_{s,7}^v(t) + S_0^w(t)i_{s,7}^w(t)\Big] + \Big[S_0^u(t)i_{s,11}^u(t) \\
& + S_0^v(t)i_{s,11}^v(t) + S_0^w(t)i_{s,11}^w(t)\Big] + \Big[S_0^u(t)i_{s,13}^u(t) + S_0^v(t)i_{s,13}^v(t) + S_0^w(t)i_{s,13}^w(t)\Big] + ... \\
& + \Big[S_1^u(t)i_{s,1}^u(t) + S_1^v(t)i_{s,1}^v(t) + S_1^w(t)i_{s,1}^w(t)\Big] + \Big[S_1^u(t)i_{s,5}^u(t) + S_1^v(t)i_{s,5}^v(t) \\
& + S_1^w(t)i_{s,5}^w(t)\Big] + \Big[S_1^u(t)i_{s,7}^u(t) + S_1^v(t)i_{s,7}^v(t) + S_1^w(t)i_{s,7}^w(t)\Big] + \Big[S_1^u(t)i_{s,11}^u(t) \\
& + S_1^v(t)i_{s,11}^v(t) + S_1^w(t)i_{s,11}^w(t)\Big] + \Big[S_1^u(t)i_{s,13}^u(t) + S_1^v(t)i_{s,13}^v(t) + S_1^w(t)i_{s,13}^w(t)\Big] + ... \\
& + \Big[S_3^u(t)i_{s,1}^u(t) + S_3^v(t)i_{s,1}^v(t) + S_3^w(t)i_{s,1}^w(t)\Big] + \Big[S_3^u(t)i_{s,5}^u(t) + S_3^v(t)i_{s,5}^v(t) \\
& + S_3^w(t)i_{s,5}^w(t)\Big] + \Big[S_3^u(t)i_{s,7}^u(t) + S_3^v(t)i_{s,7}^v(t) + S_3^w(t)i_{s,7}^w(t)\Big] + \Big[S_3^u(t)i_{s,11}^u(t) \\
& + S_3^v(t)i_{s,11}^v(t) + S_3^w(t)i_{s,11}^w(t)\Big] + \Big[S_3^u(t)i_{s,13}^u(t) + S_3^v(t)i_{s,13}^v(t) + S_3^w(t)i_{s,13}^w(t)\Big] + ... \\
& + \Big[S_5^u(t)i_{s,1}^u(t) + S_5^v(t)i_{s,1}^v(t) + S_5^w(t)i_{s,1}^w(t)\Big] + \Big[S_5^u(t)i_{s,5}^u(t) + S_5^v(t)i_{s,5}^v(t) \\
& + S_5^w(t)i_{s,5}^w(t)\Big] + \Big[S_5^u(t)i_{s,7}^u(t) + S_5^v(t)i_{s,7}^v(t) + S_5^w(t)i_{s,7}^w(t)\Big] + \Big[S_5^u(t)i_{s,11}^u(t) \\
& + S_5^v(t)i_{s,11}^v(t) + S_5^w(t)i_{s,11}^w(t)\Big] + \Big[S_5^u(t)i_{s,13}^u(t) + S_5^v(t)i_{s,13}^v(t) + S_5^w(t)i_{s,13}^w(t)\Big] + ... \\
& + \Big[S_7^u(t)i_{s,1}^u(t) + S_7^v(t)i_{s,1}^v(t) + S_7^w(t)i_{s,1}^w(t)\Big] + \Big[S_7^u(t)i_{s,5}^u(t) + S_7^v(t)i_{s,5}^v(t) \\
& + S_7^w(t)i_{s,5}^w(t)\Big] + \Big[S_7^u(t)i_{s,7}^u(t) + S_7^v(t)i_{s,7}^v(t) + S_7^w(t)i_{s,7}^w(t)\Big] + \Big[S_7^u(t)i_{s,11}^u(t) \\
& + S_7^v(t)i_{s,11}^v(t) + S_7^w(t)i_{s,11}^w(t)\Big] + \Big[S_7^u(t)i_{s,13}^u(t) + S_7^v(t)i_{s,13}^v(t) + S_7^w(t)i_{s,13}^w(t)\Big] + ... \\
& + \Big[S_9^u(t)i_{s,1}^u(t) + S_9^v(t)i_{s,1}^v(t) + S_9^w(t)i_{s,1}^w(t)\Big] + \Big[S_9^u(t)i_{s,5}^u(t) + S_9^v(t)i_{s,5}^v(t) \\
& + S_9^w(t)i_{s,5}^w(t)\Big] + \Big[S_9^u(t)i_{s,7}^u(t) + S_9^v(t)i_{s,7}^v(t) + S_9^w(t)i_{s,7}^w(t)\Big] + \Big[S_9^u(t)i_{s,11}^u(t) \\
& + S_9^v(t)i_{s,11}^v(t) + S_9^w(t)i_{s,11}^w(t)\Big] + \Big[S_9^u(t)i_{s,13}^u(t) + S_9^v(t)i_{s,13}^v(t) + S_9^w(t)i_{s,13}^w(t)\Big] + ... \\
& + \Big[S_{11}^u(t)i_{s,1}^u(t) + S_{11}^v(t)i_{s,1}^v(t) + S_{11}^w(t)i_{s,1}^w(t)\Big] + \Big[S_{11}^u(t)i_{s,5}^u(t) + S_{11}^v(t)i_{s,5}^v(t) \\
& + S_{11}^w(t)i_{s,5}^w(t)\Big] + \Big[S_{11}^u(t)i_{s,7}^u(t) + S_{11}^v(t)i_{s,7}^v(t) + S_{11}^w(t)i_{s,7}^w(t)\Big] + \Big[S_{11}^u(t)i_{s,11}^u(t) \\
& + S_{11}^v(t)i_{s,11}^v(t) + S_{11}^w(t)i_{s,11}^w(t)\Big] + \Big[S_{11}^u(t)i_{s,13}^u(t) + S_{11}^v(t)i_{s,13}^v(t) + S_{11}^w(t)i_{s,13}^w(t)\Big] + ... \\
& + ...
\end{aligned} \tag{4.11}
$$

Solving equation (4.11) and keeping in mind that the signals in phase V and W are the same as in phase U but with a phase shift of $\frac{2\pi}{3}$ and $\frac{4\pi}{3}$,respectively, many terms in equation (4.11) get simplified when the additions theorem is used for these phases.

For example:

$$
\begin{aligned}
&i_{inv\_S_0, i_{S,1}}(t) = \\
&= S_0^u(t) i_{s,1}^u(t) + S_0^v(t) i_{s,1}^v(t) + S_0^w(t) i_{s,1}^w(t) \\
&= \frac{a_0}{2}\Big[U_{DC} \frac{u_{s,0}^d + \omega_r L_s^q (u_{s,0}^q - (\omega_r \psi_{pm}))}{\omega_r^2 L_s^d L_s^q} \cos(\omega_r t) + U_{DC} \frac{u_{s,0}^d}{\omega_r L_s^q} \sin(\omega_r t) \\
&+ U_{DC} \frac{u_{s,0}^d + \omega_r L_s^q (u_{s,0}^q - (\omega_r \psi_{pm}))}{\omega_r^2 L_s^d L_s^q} \cos(\omega_r t - \frac{2\pi}{3}) + U_{DC} \frac{u_{s,0}^d}{\omega_r L_s^q} \sin(\omega_r t - \frac{2\pi}{3}) \\
&+ U_{DC} \frac{u_{s,0}^d + \omega_r L_s^q (u_{s,0}^q - (\omega_r \psi_{pm}))}{\omega_r^2 L_s^d L_s^q} \cos(\omega_r t - \frac{4\pi}{3}) + U_{DC} \frac{u_{s,0}^d}{\omega_r L_s^q} \sin(\omega_r t - \frac{4\pi}{3})\Big] \\
&= \frac{a_0}{2}\Bigg[U_{DC} \frac{u_{s,0}^d + \omega_r L_s^q (u_{s,0}^q - (\omega_r \psi_{pm}))}{\omega_r^2 L_s^d L_s^q} \Big[\cos(\omega_r t) + \cos(\omega_r t - \frac{2\pi}{3}) + \cos(\omega_r t - \frac{4\pi}{3})\Big] \\
&+ U_{DC} \frac{u_{s,0}^d}{\omega_r L_s^q} \Big[\sin(\omega_r t) + \sin(\omega_r t - \frac{2\pi}{3}) + \sin(\omega_r t - \frac{4\pi}{3})\Big]\Bigg] \\
&= \frac{a_0}{2}\Bigg[U_{DC} \frac{u_{s,0}^d + \omega_r L_s^q (u_{s,0}^q - (\omega_r \psi_{pm}))}{\omega_r^2 L_s^d L_s^q} \Big[0\Big] \\
&+ U_{DC} \frac{u_{s,0}^d}{\omega_r L_s^q} \Big[0\Big]\Bigg] \\
&= 0
\end{aligned}
\tag{4.12}
$$

Doing so for all terms of equation (4.11) leads to the knowledge that there are five groups, which are not equal to zero and so determine the inverter current $i_{inv}(t)$.This resulting current consists of a DC-part and multiples of six harmonics.
Table 4.1 represents how the DC-part is formed for the inverter current. The first

DC group 1	DC group 2
$S_1 i_{s,1}$	$S_5 i_{s,5}$
	$S_7 i_{s,7}$
	$S_{11} i_{s,11}$
	$S_{13} i_{s,13}$
	$S_{17} i_{s,17}$
	$S_{19} i_{s,19}$
	$S_{23} i_{s,23}$
	$S_{25} i_{s,25}$
	.
	.
	.

Table 4.1: *Table for calculating the DC-part of the inverter current for DC-group 1 and 2*

DC-part of the inverter current is generated by the sum of the fundamental switching waveform multiplied with the fundamental current waveform for all three phases, which results in

$$
\begin{aligned}
i_{inv\_DC1}(t) = \frac{3}{2}U_{DC}\Big[&a_1\frac{u^d_{s,0}+\omega_r L^q_s(u^q_{s,0}-(\omega_r\psi_{pm}))}{\omega_r^2 L^d_s L^q_s}\cos(\gamma)+a_1\frac{u^d_{s,0}}{\omega_r L^q_s}\sin(\gamma)\\
&+b_1\frac{u^d_{s,0}+\omega_r L^q_s(u^q_{s,0}-(\omega_r\psi_{pm}))}{\omega_r^2 L^d_s L^q_s}\sin(\gamma)-b_1\frac{u^d_{s,0}}{\omega_r L^q_s}\cos(\gamma)\Big].
\end{aligned}
\tag{4.13}
$$

The second DC-part of the inverter current is formed by the sum of all $\nu-1$ order switching harmonics, multiplied with $\nu-1$ order current harmonics and $\nu+1$ order switching harmonic, multiplied with $\nu+1$ order current harmonics for all three phases.

$$
\begin{aligned}
&i_{inv\_DC2}(t) = \frac{3}{2}U_{DC}\frac{1}{2\omega_r L^q_s}\sum_{\nu=6i}^{+\infty}\Big[\\
&\Big(\frac{a_{\nu+1}}{\nu+1}(\lambda-1)\cos(2\gamma)+\frac{a_{\nu-1}}{\nu-1}(\lambda+1)+\frac{b_{\nu+1}}{\nu+1}(\lambda-1)\sin(2\gamma)\Big)b_{\nu-1}\\
&+\Big(\frac{a_{\nu+1}}{\nu+1}(\lambda-1)\sin(2\gamma)-\frac{b_{\nu-1}}{\nu-1}(\lambda+1)-\frac{b_{\nu+1}}{\nu+1}(\lambda-1)\cos(2\gamma)\Big)a_{\nu-1}\\
&+\Big(\frac{a_{\nu-1}}{\nu-1}(\lambda-1)\cos(2\gamma)+\frac{a_{\nu+1}}{\nu+1}(\lambda+1)-\frac{b_{\nu-1}}{\nu-1}(\lambda-1)\sin(2\gamma)\Big)b_{\nu+1}\\
&+\Big(-\frac{a_{\nu-1}}{\nu-1}(\lambda-1)\sin(2\gamma)-\frac{b_{\nu+1}}{\nu+1}(\lambda+1)-\frac{b_{\nu-1}}{\nu-1}(\lambda-1)\cos(2\gamma)\Big)a_{\nu+1}\Big]
\end{aligned}
\tag{4.14}
$$

Combining (4.13) and (4.14) results in

$$
\begin{aligned}
i_{inv\_DC}(t) &= i_{inv\_DC1}(t)+i_{inv\_DC2}(t)\\
&=\frac{3}{2}U_{DC}\Big[a_1\frac{u^d_{s,0}+\omega_r L^q_s(u^q_{s,0}-(\omega_r\psi_{pm}))}{\omega_r^2 L^d_s L^q_s}\cos(\gamma)+a_1\frac{u^d_{s,0}}{\omega_r L^q_s}\sin(\gamma)\\
&+b_1\frac{u^d_{s,0}+\omega_r L^q_s(u^q_{s,0}-(\omega_r\psi_{pm}))}{\omega_r^2 L^d_s L^q_s}\sin(\gamma)-b_1\frac{u^d_{s,0}}{\omega_r L^q_s}\cos(\gamma)\Big]\\
&+\frac{3}{2}U_{DC}\frac{1}{2\omega_r L^q_s}\sum_{\nu=6i}^{+\infty}\Big[\\
&\Big(\frac{a_{\nu+1}}{\nu+1}(\lambda-1)\cos(2\gamma)+\frac{a_{\nu-1}}{\nu-1}(\lambda+1)+\frac{b_{\nu+1}}{\nu+1}(\lambda-1)\sin(2\gamma)\Big)b_{\nu-1}\\
&+\Big(\frac{a_{\nu+1}}{\nu+1}(\lambda-1)\sin(2\gamma)-\frac{b_{\nu-1}}{\nu-1}(\lambda+1)-\frac{b_{\nu+1}}{\nu+1}(\lambda-1)\cos(2\gamma)\Big)a_{\nu-1}\\
&+\Big(\frac{a_{\nu-1}}{\nu-1}(\lambda-1)\cos(2\gamma)+\frac{a_{\nu+1}}{\nu+1}(\lambda+1)-\frac{b_{\nu-1}}{\nu-1}(\lambda-1)\sin(2\gamma)\Big)b_{\nu+1}\\
&+\Big(-\frac{a_{\nu-1}}{\nu-1}(\lambda-1)\sin(2\gamma)-\frac{b_{\nu+1}}{\nu+1}(\lambda+1)-\frac{b_{\nu-1}}{\nu-1}(\lambda-1)\cos(2\gamma)\Big)a_{\nu+1}\Big].
\end{aligned}
\tag{4.15}
$$

The given tables 4.2, 4.3 and 4.4 show which parts of equation (4.11) contribute to the harmonic parts of $i_{inv}(t)$. In table 4.2 $S_5 i_{s,1}$ implies $S^u_5(t)i^u_{s,1}(t)+S^v_5(t)i^v_{s,1}(t)+$

$S_5^w(t)i_{s,1}^w(t)$.

harmonics group 1				
6. harmonic	12. harmonic	18. harmonic	24. harmonic	30. harmonic
$S_5 i_{s,1}$	$S_{11} i_{s,1}$	$S_{17} i_{s,1}$	$S_{23} i_{s,1}$	$S_{29} i_{s,1}$
$S_1 i_{s,5}$	$S_1 i_{s,11}$	$S_1 i_{s,17}$	$S_1 i_{s,23}$	$S_1 i_{s,29}$
$S_7 i_{s,1}$	$S_{13} i_{s,1}$	$S_{19} i_{s,1}$	$S_{25} i_{s,1}$	$S_{31} i_{s,1}$
$S_1 i_{s,7}$	$S_1 i_{s,13}$	$S_1 i_{s,19}$	$S_1 i_{s,25}$	$S_1 i_{s,31}$

Table 4.2: *Table for calculating the harmonic components of the inverter current of harmonics group 1*

Written as a final equation, the harmonic inverter current component produced by group 1 is

$$
\begin{aligned}
&i_{inv\_group1} = \frac{3}{2} U_{DC} \sum_{\nu=6i}^{+\infty} \Bigg[\\
&\Bigg[\frac{u_{s,0}^d + \omega_r L_s^q (u_{s,0}^q - (\omega_r \psi_{pm}))}{\omega_r^2 L_s^d L_s^q} [(a_{\nu-1} + a_{\nu+1})\cos(\gamma) + (b_{\nu+1} - b_{\nu-1})\sin(\gamma)] \\
&+ \frac{u_{s,0}^d}{\omega_r L_s^q} [(a_{\nu-1} + a_{\nu+1})\sin(\gamma) + (b_{\nu-1} - b_{\nu+1})\cos(\gamma)] \\
&+ \frac{1}{2\omega_r L_s^q} \Big[- b_1 \Big(\frac{a_{\nu+1}}{\nu+1}(\lambda-1)\cos(2\gamma) + \frac{a_{\nu-1}}{\nu-1}(\lambda+1) + \frac{b_{\nu+1}}{\nu+1}(\lambda-1)\sin(2\gamma) \Big) \\
&+ a_1 \Big(\frac{a_{\nu+1}}{\nu+1}(\lambda-1)\sin(2\gamma) - \frac{b_{\nu-1}}{\nu-1}(\lambda+1) - \frac{b_{\nu+1}}{\nu+1}(\lambda-1)\cos(2\gamma) \Big) \\
&+ b_1 \Big(\frac{a_{\nu-1}}{\nu-1}(\lambda-1)\cos(2\gamma) + \frac{a_{\nu+1}}{\nu+1}(\lambda+1) - \frac{b_{\nu-1}}{\nu-1}(\lambda-1)\sin(2\gamma) \Big) \\
&+ a_1 \Big(- \frac{a_{\nu-1}}{\nu-1}(\lambda-1)\sin(2\gamma) - \frac{b_{\nu+1}}{\nu+1}(\lambda+1) - \frac{b_{\nu-1}}{\nu-1}(\lambda-1)\cos(2\gamma) \Big) \Big] \Bigg] \\
&\cos(\nu(\omega_r t + \gamma)) \\
&+ \Bigg[\frac{u_{s,0}^d + \omega_r L_s^q (u_{s,0}^q - (\omega_r \psi_{pm}))}{\omega_r^2 L_s^d L_s^q} [(a_{\nu-1} - a_{\nu+1})\sin(\gamma) + (b_{\nu+1} + b_{\nu-1})\cos(\gamma)] \\
&+ \frac{u_{s,0}^d}{\omega_r L_s^q} [(a_{\nu+1} - a_{\nu-1})\cos(\gamma) + (b_{\nu-1} + b_{\nu+1})\sin(\gamma)] \\
&+ \frac{1}{2\omega_r L_s^q} \Big[a_1 \Big(\frac{a_{\nu+1}}{\nu+1}(\lambda-1)\cos(2\gamma) + \frac{a_{\nu-1}}{\nu-1}(\lambda+1) + \frac{b_{\nu+1}}{\nu+1}(\lambda-1)\sin(2\gamma) \Big) \\
&+ b_1 \Big(\frac{a_{\nu+1}}{\nu+1}(\lambda-1)\sin(2\gamma) - \frac{b_{\nu-1}}{\nu-1}(\lambda+1) - \frac{b_{\nu+1}}{\nu+1}(\lambda-1)\cos(2\gamma) \Big) \\
&+ a_1 \Big(\frac{a_{\nu-1}}{\nu-1}(\lambda-1)\cos(2\gamma) + \frac{a_{\nu+1}}{\nu+1}(\lambda+1) - \frac{b_{\nu-1}}{\nu-1}(\lambda-1)\sin(2\gamma) \Big) \\
&- b_1 \Big(- \frac{a_{\nu-1}}{\nu-1}(\lambda-1)\sin(2\gamma) - \frac{b_{\nu+1}}{\nu+1}(\lambda+1) - \frac{b_{\nu-1}}{\nu-1}(\lambda-1)\cos(2\gamma) \Big) \Big] \Bigg] \\
&\sin(\nu(\omega_r t + \gamma)) \Bigg].
\end{aligned}
\tag{4.16}
$$

harmonics group 2				
6. harmonic	12. harmonic	18. harmonic	24. harmonic	30. harmonic
	$S_5 i_{s,7}$ $S_7 i_{s,5}$	$S_5 i_{s,13}$ $S_{13} i_{s,5}$ $S_7 i_{s,11}$ $S_{11} i_{s,7}$	$S_5 i_{s,19}$ $S_{19} i_{s,5}$ $S_7 i_{s,17}$ $S_{17} i_{s,7}$ $S_{11} i_{s,13}$ $S_{13} i_{s,11}$	$S_5 i_{s,25}$ $S_{25} i_{s,5}$ $S_7 i_{s,23}$ $S_{23} i_{s,7}$ $S_{11} i_{s,19}$ $S_{19} i_{s,11}$ $S_{13} i_{s,17}$ $S_{17} i_{s,13}$

Table 4.3: *Table for calculating the harmonic components of the inverter current of harmonics group 2*

Written as a final equation, the harmonic inverter current component produced by group 2 is

$$
\begin{aligned}
&i_{inv\_group2} = \frac{3}{2} U_{DC} \frac{1}{2\omega_r L_s^q} \sum_{\nu=6i}^{+\infty} \sum_{k=6i}^{\nu-6} \Bigg[\\
&\Bigg[a_{k+1} \Bigg(\frac{a_{\nu-k+1}}{\nu-k+1} (\lambda-1)\cos(2\gamma) + \frac{a_{\nu-k-1}}{\nu-k-1}(\lambda+1) + \frac{b_{\nu-k+1}}{\nu-k+1}(\lambda-1)\sin(2\gamma) \Bigg) \\
&+ b_{k+1} \Bigg(\frac{a_{\nu-k+1}}{\nu-k+1} (\lambda-1)\sin(2\gamma) - \frac{b_{\nu-k-1}}{\nu-k-1}(\lambda+1) - \frac{b_{\nu-k+1}}{\nu-k+1}(\lambda-1)\cos(2\gamma) \Bigg) \\
&+ a_{k-1} \Bigg(\frac{a_{\nu-k-1}}{\nu-k-1} (\lambda-1)\cos(2\gamma) + \frac{a_{\nu-k+1}}{\nu-k+1}(\lambda+1) - \frac{b_{\nu-k-1}}{\nu-k-1}(\lambda-1)\sin(2\gamma) \Bigg) \\
&+ b_{k-1} \Bigg(-\frac{a_{\nu-k-1}}{\nu-k-1} (\lambda-1)\sin(2\gamma) - \frac{b_{\nu-k+1}}{\nu-k+1}(\lambda+1) - \frac{b_{\nu-k-1}}{\nu-k-1}(\lambda-1)\cos(2\gamma) \Bigg) \Bigg] \\
&\sin(\nu(\omega_r t + \gamma)) \\
&- \Bigg[b_{k+1} \Bigg(\frac{a_{\nu-k+1}}{\nu-k+1} (\lambda-1)\cos(2\gamma) + \frac{a_{\nu-k-1}}{\nu-k-1}(\lambda+1) + \frac{b_{\nu-k+1}}{\nu-k+1}(\lambda-1)\sin(2\gamma) \Bigg) \\
&- a_{k+1} \Bigg(\frac{a_{\nu-k+1}}{\nu-k+1} (\lambda-1)\sin(2\gamma) - \frac{b_{\nu-k-1}}{\nu-k-1}(\lambda+1) - \frac{b_{\nu-k+1}}{\nu-k+1}(\lambda-1)\cos(2\gamma) \Bigg) \\
&+ b_{k-1} \Bigg(\frac{a_{\nu-k-1}}{\nu-k-1} (\lambda-1)\cos(2\gamma) + \frac{a_{\nu-k+1}}{\nu-k+1}(\lambda+1) - \frac{b_{\nu-k-1}}{\nu-k-1}(\lambda-1)\sin(2\gamma) \Bigg) \\
&- a_{k-1} \Bigg(-\frac{a_{\nu-k-1}}{\nu-k-1} (\lambda-1)\sin(2\gamma) - \frac{b_{\nu-k+1}}{\nu-k+1}(\lambda+1) - \frac{b_{\nu-k-1}}{\nu-k-1}(\lambda-1)\cos(2\gamma) \Bigg) \Bigg] \\
&\cos(\nu(\omega_r t + \gamma)) \Bigg].
\end{aligned}
\tag{4.17}
$$

harmonics group 3				
6. harmonic	12. harmonic	18. harmonic	24. harmonic	30. harmonic
$S_5 i_{s,11}$	$S_5 i_{s,17}$	$S_5 i_{s,23}$	$S_5 i_{s,29}$	$S_5 i_{s,35}$
$S_{11} i_{s,5}$	$S_{17} i_{s,5}$	$S_{23} i_{s,5}$	$S_{29} i_{s,5}$	$S_{35} i_{s,5}$
$S_7 i_{s,13}$	$S_7 i_{s,19}$	$S_7 i_{s,25}$	$S_7 i_{s,31}$	$S_7 i_{s,37}$
$S_{13} i_{s,7}$	$S_{19} i_{s,7}$	$S_{25} i_{s,7}$	$S_{31} i_{s,7}$	$S_{37} i_{s,7}$
$S_{11} i_{s,17}$	$S_{11} i_{s,23}$	$S_{11} i_{s,29}$	$S_{11} i_{s,35}$	$S_{11} i_{s,41}$
$S_{17} i_{s,11}$	$S_{23} i_{s,11}$	$S_{29} i_{s,11}$	$S_{35} i_{s,11}$	$S_{41} i_{s,11}$
$S_{13} i_{s,19}$	$S_{13} i_{s,25}$	$S_{13} i_{s,31}$	$S_{13} i_{s,37}$	$S_{13} i_{s,43}$
$S_{19} i_{s,13}$	$S_{25} i_{s,13}$	$S_{31} i_{s,13}$	$S_{37} i_{s,13}$	$S_{43} i_{s,13}$
.	.	.	.	.
.	.	.	.	.
.	.	.	.	.

Table 4.4: *Table for calculating the harmonic components of the inverter current of harmonics group 3*

Written as a final equation, the harmonic inverter current component produced by group 3 is

$$
\begin{aligned}
i_{inv\_group3} &= \frac{3}{2} U_{DC} \frac{1}{2\omega_r L_s^q} \sum_{\nu=6i}^{+\infty} \sum_{j=6i}^{+\infty} \Bigg[\\
&\Bigg[b_{j-1} \Big(\frac{a_{\nu+j+1}}{\nu+j+1}(\lambda-1)\cos(2\gamma) + \frac{a_{\nu+j-1}}{\nu+j-1}(\lambda+1) + \frac{b_{\nu+j+1}}{\nu+j+1}(\lambda-1)\sin(2\gamma) \Big) \\
&+ a_{j-1} \Big(\frac{a_{\nu+j+1}}{\nu+j+1}(\lambda-1)\sin(2\gamma) - \frac{b_{\nu+j-1}}{\nu+j-1}(\lambda+1) - \frac{b_{\nu+j+1}}{\nu+j+1}(\lambda-1)\cos(2\gamma) \Big) \\
&+ b_{j-1+\nu} \Big(\frac{a_{j+1}}{j+1}(\lambda-1)\cos(2\gamma) + \frac{a_{j-1}}{j-1}(\lambda+1) + \frac{b_{j+1}}{j+1}(\lambda-1)\sin(2\gamma) \Big) \\
&+ a_{j-1+\nu} \Big(\frac{a_{j+1}}{j+1}(\lambda-1)\sin(2\gamma) - \frac{b_{j-1}}{j-1}(\lambda+1) - \frac{b_{j+1}}{j+1}(\lambda-1)\cos(2\gamma) \Big) \\
&+ b_{j+1} \Big(\frac{a_{\nu+j-1}}{\nu+j-1}(\lambda-1)\cos(2\gamma) + \frac{a_{\nu+j+1}}{\nu+j+1}(\lambda+1) - \frac{b_{\nu+j-1}}{\nu+j-1}(\lambda-1)\sin(2\gamma) \Big) \\
&+ a_{j+1} \Big(-\frac{a_{\nu+j-1}}{\nu+j-1}(\lambda-1)\sin(2\gamma) - \frac{b_{\nu+j+1}}{\nu+j+1}(\lambda+1) - \frac{b_{\nu+j-1}}{\nu+j-1}(\lambda-1)\cos(2\gamma) \Big) \\
&+ b_{j+1+\nu} \Big(\frac{a_{j-1}}{j-1}(\lambda-1)\cos(2\gamma) + \frac{a_{j+1}}{j+1}(\lambda+1) - \frac{b_{j-1}}{j-1}(\lambda-1)\sin(2\gamma) \Big) \\
&+ a_{j+1+\nu} \Big(-\frac{a_{j-1}}{j-1}(\lambda-1)\sin(2\gamma) - \frac{b_{j+1}}{j+1}(\lambda+1) - \frac{b_{j-1}}{j-1}(\lambda-1)\cos(2\gamma) \Big) \Bigg] \\
&\cos(\nu(\omega_r t + \gamma)) \\
&+ \Bigg[a_{j-1} \Big(\frac{a_{\nu+j+1}}{\nu+j+1}(\lambda-1)\cos(2\gamma) + \frac{a_{\nu+j-1}}{\nu+j-1}(\lambda+1) + \frac{b_{\nu+j+1}}{\nu+j+1}(\lambda-1)\sin(2\gamma) \Big) \\
&- b_{j-1} \Big(\frac{a_{\nu+j+1}}{\nu+j+1}(\lambda-1)\sin(2\gamma) - \frac{b_{\nu+j-1}}{\nu+j-1}(\lambda+1) - \frac{b_{\nu+j+1}}{\nu+j+1}(\lambda-1)\cos(2\gamma) \Big)
\end{aligned}
$$

$$
\begin{aligned}
&- a_{j-1+\nu}\Big(\frac{a_{j+1}}{j+1}(\lambda-1)\cos(2\gamma)+\frac{a_{j-1}}{j-1}(\lambda+1)+\frac{b_{j+1}}{j+1}(\lambda-1)\sin(2\gamma)\Big)\\
&+ b_{j-1+\nu}\Big(\frac{a_{j+1}}{j+1}(\lambda-1)\sin(2\gamma)-\frac{b_{j-1}}{j-1}(\lambda+1)-\frac{b_{j+1}}{j+1}(\lambda-1)\cos(2\gamma)\Big)\\
&+ a_{j+1}\Big(\frac{a_{\nu+j-1}}{\nu+j-1}(\lambda-1)\cos(2\gamma)+\frac{a_{\nu+j+1}}{\nu+j+1}(\lambda+1)-\frac{b_{\nu+j-1}}{\nu+j-1}(\lambda-1)\sin(2\gamma)\Big)\\
&- b_{j+1}\Big(-\frac{a_{\nu+j-1}}{\nu+j-1}(\lambda-1)\sin(2\gamma)-\frac{b_{\nu+j+1}}{\nu+j+1}(\lambda+1)-\frac{b_{\nu+j-1}}{\nu+j-1}(\lambda-1)\cos(2\gamma)\Big)\\
&- a_{j+1+\nu}\Big(\frac{a_{j-1}}{j-1}(\lambda-1)\cos(2\gamma)+\frac{a_{j+1}}{j+1}(\lambda+1)-\frac{b_{j-1}}{j-1}(\lambda-1)\sin(2\gamma)\Big)\\
&+ b_{j+1+\nu}\Big(-\frac{a_{j-1}}{j-1}(\lambda-1)\sin(2\gamma)-\frac{b_{j+1}}{j+1}(\lambda+1)-\frac{b_{j-1}}{j-1}(\lambda-1)\cos(2\gamma)\Big)\Big]\\
&\sin(\nu(\omega_r t+\gamma))\Big].
\end{aligned}
$$

Combining and rearranging the harmonic groups while separating them for a sine and cosine part, the equations (4.18) and (4.19) are found.

$$\begin{aligned}
i_{inv_cos,\nu}(t) = \frac{3}{2}U_{DC}\Bigg[& \frac{u^d_{s,0}+\omega_r L^q_s(u^q_{s,0}-(\omega_r\psi_{pm}))}{\omega_r^2 L^d_s L^q_s} \\
& [(a_{\nu-1}+a_{\nu+1})\cos(\gamma)+(b_{\nu+1}-b_{\nu-1})\sin(\gamma)] \\
& + \frac{u^d_{s,0}}{\omega_r L^q_s}[(a_{\nu-1}+a_{\nu+1})\sin(\gamma)+(b_{\nu-1}-b_{\nu+1})\cos(\gamma)] \\
& + \frac{1}{2\omega_r L^q_s}\Bigg[\Big[-b_1\Big(\frac{a_{\nu+1}}{\nu+1}(\lambda-1)\cos(2\gamma)+\frac{a_{\nu-1}}{\nu-1}(\lambda+1)+\frac{b_{\nu+1}}{\nu+1}(\lambda-1)\sin(2\gamma)\Big) \\
& + a_1\Big(\frac{a_{\nu+1}}{\nu+1}(\lambda-1)\sin(2\gamma)-\frac{b_{\nu-1}}{\nu-1}(\lambda+1)-\frac{b_{\nu+1}}{\nu+1}(\lambda-1)\cos(2\gamma)\Big) \\
& + b_1\Big(\frac{a_{\nu-1}}{\nu-1}(\lambda-1)\cos(2\gamma)+\frac{a_{\nu+1}}{\nu+1}(\lambda+1)-\frac{b_{\nu-1}}{\nu-1}(\lambda-1)\sin(2\gamma)\Big) \\
& + a_1\Big(-\frac{a_{\nu-1}}{\nu-1}(\lambda-1)\sin(2\gamma)-\frac{b_{\nu+1}}{\nu+1}(\lambda+1)-\frac{b_{\nu-1}}{\nu-1}(\lambda-1)\cos(2\gamma)\Big)\Big] \\
& - \sum_{k=6i}^{\nu-6}\Big[b_{k+1}\Big(\frac{a_{\nu-k+1}}{\nu-k+1}(\lambda-1)\cos(2\gamma)+\frac{a_{\nu-k-1}}{\nu-k-1}(\lambda+1)+\frac{b_{\nu-k+1}}{\nu-k+1}(\lambda-1)\sin(2\gamma)\Big) \\
& - a_{k+1}\Big(\frac{a_{\nu-k+1}}{\nu-k+1}(\lambda-1)\sin(2\gamma)-\frac{b_{\nu-k-1}}{\nu-k-1}(\lambda+1)-\frac{b_{\nu-k+1}}{\nu-k+1}(\lambda-1)\cos(2\gamma)\Big) \\
& + b_{k-1}\Big(\frac{a_{\nu-k-1}}{\nu-k-1}(\lambda-1)\cos(2\gamma)+\frac{a_{\nu-k+1}}{\nu-k+1}(\lambda+1)-\frac{b_{\nu-k-1}}{\nu-k-1}(\lambda-1)\sin(2\gamma)\Big) \\
& - a_{k-1}\Big(-\frac{a_{\nu-k-1}}{\nu-k-1}(\lambda-1)\sin(2\gamma)-\frac{b_{\nu-k+1}}{\nu-k+1}(\lambda+1)-\frac{b_{\nu-k-1}}{\nu-k-1}(\lambda-1)\cos(2\gamma)\Big)\Big] \\
& + \sum_{j=6i}^{+\infty}\Big[b_{j-1}\Big(\frac{a_{\nu+j+1}}{\nu+j+1}(\lambda-1)\cos(2\gamma)+\frac{a_{\nu+j-1}}{\nu+j-1}(\lambda+1)+\frac{b_{\nu+j+1}}{\nu+j+1}(\lambda-1)\sin(2\gamma)\Big) \\
& + a_{j-1}\Big(\frac{a_{\nu+j+1}}{\nu+j+1}(\lambda-1)\sin(2\gamma)-\frac{b_{\nu+j-1}}{\nu+j-1}(\lambda+1)-\frac{b_{\nu+j+1}}{\nu+j+1}(\lambda-1)\cos(2\gamma)\Big) \\
& + b_{j-1+\nu}\Big(\frac{a_{j+1}}{j+1}(\lambda-1)\cos(2\gamma)+\frac{a_{j-1}}{j-1}(\lambda+1)+\frac{b_{j+1}}{j+1}(\lambda-1)\sin(2\gamma)\Big) \\
& + a_{j-1+\nu}\Big(\frac{a_{j+1}}{j+1}(\lambda-1)\sin(2\gamma)-\frac{b_{j-1}}{j-1}(\lambda+1)-\frac{b_{j+1}}{j+1}(\lambda-1)\cos(2\gamma)\Big) \\
& + b_{j+1}\Big(\frac{a_{\nu+j-1}}{\nu+j-1}(\lambda-1)\cos(2\gamma)+\frac{a_{\nu+j+1}}{\nu+j+1}(\lambda+1)-\frac{b_{\nu+j-1}}{\nu+j-1}(\lambda-1)\sin(2\gamma)\Big) \\
& + a_{j+1}\Big(-\frac{a_{\nu+j-1}}{\nu+j-1}(\lambda-1)\sin(2\gamma)-\frac{b_{\nu+j+1}}{\nu+j+1}(\lambda+1)-\frac{b_{\nu+j-1}}{\nu+j-1}(\lambda-1)\cos(2\gamma)\Big) \\
& + b_{j+1+\nu}\Big(\frac{a_{j-1}}{j-1}(\lambda-1)\cos(2\gamma)+\frac{a_{j+1}}{j+1}(\lambda+1)-\frac{b_{j-1}}{j-1}(\lambda-1)\sin(2\gamma)\Big) \\
& + a_{j+1+\nu}\Big(-\frac{a_{j-1}}{j-1}(\lambda-1)\sin(2\gamma)-\frac{b_{j+1}}{j+1}(\lambda+1)-\frac{b_{j-1}}{j-1}(\lambda-1)\cos(2\gamma)\Big)\Big]\Bigg]\Bigg]
\end{aligned} \tag{4.18}$$

$$
\begin{aligned}
i_{inv\_sin,\nu}(t) = \frac{3}{2}U_{DC}\Bigg[&\frac{u^d_{s,0} + \omega_r L^q_s(u^q_{s,0} - (\omega_r\psi_{pm}))}{\omega_r^2 L^d_s L^q_s} \\
&[(a_{\nu-1} - a_{\nu+1})\sin(\gamma) + (b_{\nu+1} + b_{\nu-1})\cos(\gamma)] \\
&+ \frac{u^d_{s,0}}{\omega_r L^q_s}[(a_{\nu+1} - a_{\nu-1})\cos(\gamma) + (b_{\nu-1} + b_{\nu+1})\sin(\gamma)] \\
&+ \frac{1}{2\omega_r L^q_s}\Bigg[\Bigg[a_1\Big(\frac{a_{\nu+1}}{\nu+1}(\lambda-1)\cos(2\gamma) + \frac{a_{\nu-1}}{\nu-1}(\lambda+1) + \frac{b_{\nu+1}}{\nu+1}(\lambda-1)\sin(2\gamma)\Big) \\
&+ b_1\Big(\frac{a_{\nu+1}}{\nu+1}(\lambda-1)\sin(2\gamma) - \frac{b_{\nu-1}}{\nu-1}(\lambda+1) - \frac{b_{\nu+1}}{\nu+1}(\lambda-1)\cos(2\gamma)\Big) \\
&+ a_1\Big(\frac{a_{\nu-1}}{\nu-1}(\lambda-1)\cos(2\gamma) + \frac{a_{\nu+1}}{\nu+1}(\lambda+1) - \frac{b_{\nu-1}}{\nu-1}(\lambda-1)\sin(2\gamma)\Big) \\
&- b_1\Big(-\frac{a_{\nu-1}}{\nu-1}(\lambda-1)\sin(2\gamma) - \frac{b_{\nu+1}}{\nu+1}(\lambda+1) - \frac{b_{\nu-1}}{\nu-1}(\lambda-1)\cos(2\gamma)\Big)\Bigg] \\
+\sum_{k=6i}^{\nu-6}&\Bigg[a_{k+1}\Big(\frac{a_{\nu-k+1}}{\nu-k+1}(\lambda-1)\cos(2\gamma) + \frac{a_{\nu-k-1}}{\nu-k-1}(\lambda+1) + \frac{b_{\nu-k+1}}{\nu-k+1}(\lambda-1)\sin(2\gamma)\Big) \\
&+ b_{k+1}\Big(\frac{a_{\nu-k+1}}{\nu-k+1}(\lambda-1)\sin(2\gamma) - \frac{b_{\nu-k-1}}{\nu-k-1}(\lambda+1) - \frac{b_{\nu-k+1}}{\nu-k+1}(\lambda-1)\cos(2\gamma)\Big) \\
&+ a_{k-1}\Big(\frac{a_{\nu-k-1}}{\nu-k-1}(\lambda-1)\cos(2\gamma) + \frac{a_{\nu-k+1}}{\nu-k+1}(\lambda+1) - \frac{b_{\nu-k-1}}{\nu-k-1}(\lambda-1)\sin(2\gamma)\Big) \\
&+ b_{k-1}\Big(-\frac{a_{\nu-k-1}}{\nu-k-1}(\lambda-1)\sin(2\gamma) - \frac{b_{\nu-k+1}}{\nu-k+1}(\lambda+1) - \frac{b_{\nu-k-1}}{\nu-k-1}(\lambda-1)\cos(2\gamma)\Big)\Bigg] \\
+\sum_{j=6i}^{+\infty}&\Bigg[a_{j-1}\Big(\frac{a_{\nu+j+1}}{\nu+j+1}(\lambda-1)\cos(2\gamma) + \frac{a_{\nu+j-1}}{\nu+j-1}(\lambda+1) + \frac{b_{\nu+j+1}}{\nu+j+1}(\lambda-1)\sin(2\gamma)\Big) \\
&- b_{j-1}\Big(\frac{a_{\nu+j+1}}{\nu+j+1}(\lambda-1)\sin(2\gamma) - \frac{b_{\nu+j-1}}{\nu+j-1}(\lambda+1) - \frac{b_{\nu+j+1}}{\nu+j+1}(\lambda-1)\cos(2\gamma)\Big) \\
&- a_{j-1+\nu}\Big(\frac{a_{j+1}}{j+1}(\lambda-1)\cos(2\gamma) + \frac{a_{j-1}}{j-1}(\lambda+1) + \frac{b_{j+1}}{j+1}(\lambda-1)\sin(2\gamma)\Big) \\
&+ b_{j-1+\nu}\Big(\frac{a_{j+1}}{j+1}(\lambda-1)\sin(2\gamma) - \frac{b_{j-1}}{j-1}(\lambda+1) - \frac{b_{j+1}}{j+1}(\lambda-1)\cos(2\gamma)\Big) \\
&+ a_{j+1}\Big(\frac{a_{\nu+j-1}}{\nu+j-1}(\lambda-1)\cos(2\gamma) + \frac{a_{\nu+j+1}}{\nu+j+1}(\lambda+1) - \frac{b_{\nu+j-1}}{\nu+j-1}(\lambda-1)\sin(2\gamma)\Big) \\
&- b_{j+1}\Big(-\frac{a_{\nu+j-1}}{\nu+j-1}(\lambda-1)\sin(2\gamma) - \frac{b_{\nu+j+1}}{\nu+j+1}(\lambda+1) - \frac{b_{\nu+j-1}}{\nu+j-1}(\lambda-1)\cos(2\gamma)\Big) \\
&- a_{j+1+\nu}\Big(\frac{a_{j-1}}{j-1}(\lambda-1)\cos(2\gamma) + \frac{a_{j+1}}{j+1}(\lambda+1) - \frac{b_{j-1}}{j-1}(\lambda-1)\sin(2\gamma)\Big) \\
&+ b_{j+1+\nu}\Big(-\frac{a_{j-1}}{j-1}(\lambda-1)\sin(2\gamma) - \frac{b_{j+1}}{j+1}(\lambda+1) - \frac{b_{j-1}}{j-1}(\lambda-1)\cos(2\gamma)\Big)\Bigg]\Bigg]\Bigg]
\end{aligned}
\tag{4.19}
$$

Finally, the inverter current with its five components can be written as

$$
\begin{aligned}
i_{inv}(t) =& i_{inv\_DC1} + i_{inv\_DC2} + i_{inv\_group1} + i_{inv\_group2} + i_{inv\_group3} \\
=& \frac{3}{2}U_{DC}\Big[a_1 \frac{u_{s,0}^d + \omega_r L_s^q (u_{s,0}^q - (\omega_r \psi_{pm}))}{\omega_r^2 L_s^d L_s^q} \cos(\gamma) + a_1 \frac{u_{s,0}^d}{\omega_r L_s^q} \sin(\gamma) \\
&+ b_1 \frac{u_{s,0}^d + \omega_r L_s^q (u_{s,0}^q - (\omega_r \psi_{pm}))}{\omega_r^2 L_s^d L_s^q} \sin(\gamma) - b_1 \frac{u_{s,0}^d}{\omega_r L_s^q} \cos(\gamma)\Big] \\
&+ \frac{3}{2}U_{DC} \frac{1}{2\omega_r L_s^q} \sum_{\nu=6i}^{+\infty} \Bigg[\\
&\Big(\frac{a_{\nu+1}}{\nu+1}(\lambda-1)\cos(2\gamma) + \frac{a_{\nu-1}}{\nu-1}(\lambda+1) + \frac{b_{\nu+1}}{\nu+1}(\lambda-1)\sin(2\gamma)\Big) b_{\nu-1} \\
&+ \Big(\frac{a_{\nu+1}}{\nu+1}(\lambda-1)\sin(2\gamma) - \frac{b_{\nu-1}}{\nu-1}(\lambda+1) - \frac{b_{\nu+1}}{\nu+1}(\lambda-1)\cos(2\gamma)\Big) a_{\nu-1} \\
&+ \Big(\frac{a_{\nu-1}}{\nu-1}(\lambda-1)\cos(2\gamma) + \frac{a_{\nu+1}}{\nu+1}(\lambda+1) - \frac{b_{\nu-1}}{\nu-1}(\lambda-1)\sin(2\gamma)\Big) b_{\nu+1} \\
&+ \Big(-\frac{a_{\nu-1}}{\nu-1}(\lambda-1)\sin(2\gamma) - \frac{b_{\nu+1}}{\nu+1}(\lambda+1) - \frac{b_{\nu-1}}{\nu-1}(\lambda-1)\cos(2\gamma)\Big) a_{\nu+1}\Bigg] \\
&+ \sum_{\nu=6i}^{+\infty} \Big[i_{inv\_cos,\nu}(t) \cos(\nu(\omega t + \gamma)) + i_{inv\_sin,\nu}(t) \sin(\nu(\omega t + \gamma)) \Big].
\end{aligned}
\tag{4.20}
$$

Chapter 5

Derivation of the DC-link Current of the VSI

Analysing the equivalent circuit diagram of the two-level VSI (see figure 2.1) and combining R_i and R_l to R_1 as well as L_i and L_l to L_1 leads to the complex impedances $Z_{1,\nu} = R_1 + j\nu\omega_r L_1$ and $Z_{c,\nu} = R_{ESR} - j\frac{1}{\nu\omega_r C_{DC}}$. By applying Kirchhoff's law under the simplification that the DC-link voltage is constant for the phase current calculation $i_s^u(t)$, $i_s^v(t)$ and $i_s^w(t)$ the following equations are found.

$$0 = -U_0 + Z_{1,\nu} i_{b\nu}(t) + u_{DC,\nu}(t) \tag{5.1}$$

$$u_{DC,\nu}(t) = i_{c,\nu}(t) Z_{c,\nu} \tag{5.2}$$

$$i_{b,\nu}(t) = i_{inv,\nu}(t) + i_{c,\nu}(t) \tag{5.3}$$

Inserting (5.2) and (5.3) in (5.1) leads to the final equation for $i_c(t)$.

$$\begin{aligned} i_{c,\nu}(t) &= \frac{U_0}{Z_{1,\nu} + Z_{c,\nu}} - \frac{Z_{1,\nu}}{Z_{1,\nu} + Z_{c,\nu}} i_{inv,\nu}(t) \\ &= \frac{U_0}{R_1 + j\nu\omega_r L_1 + R_{ESR} - j\frac{1}{\nu\omega_r C_{DC}}} - \frac{R_1 + j\nu\omega_r L_1}{R_1 + j\nu\omega_r L_1 + R_{ESR} - j\frac{1}{\nu\omega_r C_{DC}}} i_{inv,\nu}(t) \end{aligned} \tag{5.4}$$

To eliminate the imaginary part in the denominator the complex conjugate term is multiplied and $i_c(t)$ results in:

$$\begin{aligned} i_{c,\nu}(t) = &\frac{U_0(R_1 + R_{ESR} - j(\nu\omega_r L_1 - \frac{1}{\nu\omega_r C_{DC}}))}{(R_1 + R_{ESR})^2 + (\nu\omega_r L_1 - \frac{1}{\nu\omega_r C_{DC}})^2} \\ &- \frac{R_1(R_1 + R_{ESR}) + \nu^2\omega_r^2 L_1^2 - \frac{L_1}{C_{DC}}}{(R_1 + R_{ESR})^2 + (\nu\omega_r L_1 - \frac{1}{\nu\omega_r C_{DC}})^2} i_{inv,\nu}(t) \\ &- j\frac{\nu\omega_r L_1(R_1 + R_{ESR}) - R_1(\nu\omega_r L_1 - \frac{1}{\nu\omega_r C_{DC}})}{(R_1 + R_{ESR})^2 + (\nu\omega_r L_1 - \frac{1}{\nu\omega_r C_{DC}})^2} i_{inv,\nu}(t) \end{aligned} \tag{5.5}$$

To calculate the DC-part of this equation, ν must be set to zero. In doing so, it quickly becomes clear that $i_{c,0}$ is also zero. This is an indication that equation (5.5) is correct, because by applying a pure DC voltage to a capacitor in reality, no current will flow into the capacitor after it is charged. Due to the fact that U_0 is $400V$ for $\nu = 0$ and zero for all other values for ν, the equation (5.5) can be reduced to:

$$\begin{aligned} i_c(t) = -\sum_{\nu=1}^{\infty} \Big[& \frac{R_1(R_1+R_{ESR}) + \nu^2\omega_r^2 L_1^2 - \frac{L_1}{C_{DC}}}{(R_1+R_{ESR})^2 + (\nu\omega_r L_1 - \frac{1}{\nu\omega_r C_{DC}})^2} i_{inv,\nu}(t) \\ & + j\frac{\nu\omega_r L_1(R_1+R_{ESR}) - R_1(\nu\omega_r L_1 - \frac{1}{\nu\omega_r C_{DC}})}{(R_1+R_{ESR})^2 + (\nu\omega_r L_1 - \frac{1}{\nu\omega_r C_{DC}})^2} i_{inv,\nu}(t) \Big] \end{aligned} \tag{5.6}$$

Transforming equation (5.6) into polar form and multiplying with the polar form of equation 4.20 for $\nu \geq 1$ results in

$$\begin{aligned} I_c &= -\sum_{\nu=6i}^{\infty} \Big[(\frac{3}{2}|i_{inv\_cos,\nu}(t)| \angle \nu\gamma + \frac{3}{2}|i_{inv\_sin,\nu}|(t) \angle (\nu\gamma - \frac{\pi}{2})) H_{CH,\nu} \angle \theta_{CH,\nu} \Big] \\ &= -\sum_{\nu=6i}^{\infty} \Big[\frac{3}{2} H_{ch,\nu} |i_{inv\_cos,\nu}(t)| \angle (\nu\gamma + \theta_{CH,\nu}) + \frac{3}{2} H_{ch,\nu} |i_{inv\_sin,\nu}|(t) \angle (\nu\gamma - \frac{\pi}{2} + \theta_{CH,\nu}) \Big], \end{aligned} \tag{5.7}$$

where

$$H_{CH,\nu} = \frac{\sqrt{(R_1(R_1+R_{ESR}) + \nu^2\omega_r^2 L_1^2 - \frac{L_1}{C_{DC}})^2 + (\nu\omega_r L_1(R_1+R_{ESR}) - R_1(\nu\omega_r L_1 - \frac{1}{\nu\omega_r C_{DC}}))^2}}{(R_1+R_{ESR})^2 + (\nu\omega_r L_1 - \frac{1}{\nu\omega_r C_{DC}})^2} \tag{5.8}$$

and

$$\theta_{CH,\nu} = \arctan \frac{\nu\omega_r L_1(R_1+R_{ESR}) - R_1(\nu\omega_r L_1 - \frac{1}{\nu\omega_r C_{DC}})}{R_1(R_1+R_{ESR}) + \nu\omega_r^2 L_1^2 - \frac{L_1}{C_{DC}}}. \tag{5.9}$$

Applying the phasor theory, the capacitor current (5.7) can be re-transformed into the time domain

$$\begin{aligned} i_c(t) = -\sum_{\nu=6i}^{\infty} \Big[& \frac{3}{2} H_{CH,\nu} |i_{inv\_cos,\nu}(t)| \cos(\nu(\omega t + \gamma) + \theta_{CH,\nu}) \\ & + \frac{3}{2} H_{CH,\nu} |i_{inv\_sin,\nu}(t)| \cos(\nu(\omega t + \gamma) - \frac{\pi}{2} + \theta_{CH,\nu}) \Big]. \end{aligned} \tag{5.10}$$

In general the root main square of a harmonic signal is calculated by

$$RMS_{total} = \sqrt{RMS_1^2 + RMS_2^2 + \cdots + RMS_{\nu\_max}^2} \tag{5.11}$$

where

$$RMS_\nu = \frac{\sqrt{A_{cos}^2 + A_{sin}^2}}{\sqrt{2}} = \frac{\sqrt{(\frac{3}{2} H_{CH,\nu} |i_{inv\_cos,\nu}(t)|)^2 + (\frac{3}{2} H_{CH,\nu} |i_{inv\_sin,\nu}(t)|)^2}}{\sqrt{2}}. \tag{5.12}$$

The nominator of equation (5.12) describes the magnitude of the resulting signal consisting of the sine and cosine part of the capacitor current. The denominator is the conversion factor for a sinusoidal signal form.

$$I_{c,RMS} = \sqrt{\sum_{\nu=6i}^{\infty} \frac{((\frac{3}{2} H_{CH,\nu} |i_{inv\_cos,\nu}(t)|)^2 + (\frac{3}{2} H_{CH,\nu} |i_{inv\_sin,\nu}(t)|)^2)}{2}} \tag{5.13}$$

Chapter 6

Optimization of the Switching Angles

To gain the optimized pulse patterns (OPP), a certain mathematical optimization criterion in relation to the switching angles must be determined. To optimize this criterion the function must be minimized or maximized while fulfilling all given constraints. In the most cases the THD current in the output signal is minimized to gain a sinusoidal current. This reduces further copper losses in the machine and improves the drive system efficiency [2],[5],[6],[3]. Moreover, other optimization criteria like EMC-emission reduction [9], torque ripple reduction [8], sound-emission cutback and RMS DC-link current minimization, which is used in this thesis as optimization criterion, find also application.

6.1 Optimization Criterion

The most sensible component in a VSI is the DC-link capacitor. Due to ageing, the capacitor's electrolyte dries out and leads to a breakdown of the whole VSI. This ageing phenomenon is accelerated by high temperatures, either produced in the capacitor itself or by the surrounding environment.
The ambient temperature depends on the climate, place of use of the machine, as well as the cooling strategy. These will not change with optimized switching patterns, and therefore will not be discussed further.
The heat produces in the capacitor depends on the switching strategy. To minimize the amount of heat produced, the optimization criterion for this thesis minimizes the RMS DC-link current, because $P_v = I_{c,RMS}^2 R_{ESR}$. Therefore it is very important to use a high quality capacitor with a low R_{ESR}, and most importantly, a low $I_{c,RMS}$ amplitude.
Compared to the other components in a VSI, the capacitor is relatively large, in order to maintain a more or less constant DC-link voltage during operation. Therefore it must be able to deliver high current peaks to minimize the voltage ripple in the DC-link. To supply the system with high current peaks during operation, the capacitor must have a high capacity value combined with the electric strength, which results in a large and expensive component. If the lifespan is not the focus of optimization but the cost and size reduction is the main goal, it is also possible, with the same

OPP to reduce the size and value of the capacitor by same voltage ripple in the DC-link and same lifespan. This size and cost reduction is possible due to the lower DC-current ripple in the capacitor while using the OPP.
In the previous chapters the current in the DC-link is derived in relation to the four independent switching angles (α_1-α_4).

$$I_{c,RMS} = \sqrt{\sum_{\nu=6i}^{\infty} \frac{((\frac{3}{2}H_{CH,\nu}|i_{inv\_cos,\nu}(t)|)^2 + (\frac{3}{2}H_{CH,\nu}|i_{inv\_sin,\nu}(t)|)^2)}{2}} \tag{6.1}$$

Thereafter, the optimization problem can be formulated as follows:

$$\min_{\alpha_1,\alpha_2,\alpha_3,\alpha_4} I_{c,RMS} \tag{6.2}$$

To minimize this function the following constraints need to be taken into account.

6.2 Constraints

The four independent switching angles are located in the first half electrical period of the switching signal for HWS PWM-voltages, where

$$0 \leqslant \alpha_1 \leqslant \alpha_2 \leqslant \alpha_3 \leqslant \alpha_4 \leqslant \pi. \tag{6.3}$$

Further,

$$\sqrt{a_1^2 + b_1^2} = m\frac{U_{DC}}{2} \tag{6.4}$$

must be fulfilled at any time, where a_1 and b_1 are the amplitudes of the Fourier coefficients for the fundamental voltage, m is the modulation index and U_{DC} is the DC-link voltage.

6.3 Optimization Procedure

The optimization procedure is the key to find the optimal pulse patterns, but it is not as easy as it may seams to find a global minimum of the optimization function. In this thesis Matlab combined with the **fmincon** minimization function was used. The **fmincon** function is very sensitive to the start values because it starts looking for a local minimum in the surrounding of this point. Knowing that, the optimization algorithm needs to start near the global minimum, which of course is not known yet. Therefore in this thesis a pre-optimization was executed to find the area where the global minimum is. This algorithm is designed to test all possible angles for one operating point, where the anisotropy factor, load voltage phase, modulation index and the motor speed are constant. To reduce the calculation time the angle-steps are set to 0.1745. For every step an optimization is executed with the **fmincon** function and the constraints mentioned above. At the end of this algorithm the minimum value with the responsible angles is found and can be used as a start value for the main optimization over the whole range of θ_U. Despite the relatively huge angle-steps the pre-optimization, with a capable computer, runs for several hours. This fact indicates the main problem. In order to find the global minimum for every operating point and small steps for the load voltage phase, motor speed, modulation index and anisotropy factor, a conventional computer would calculate for hundreds of years. In future such minimization problems could be faced with a quantum-computer.

Even if all global minimums where found, it is not certain whether those pulse patterns would be able to be implemented in a controllable current control loop. If the pulse patterns change drastically between two operating points, the whole current control loop becomes unstable while crossing this area during operation.

To overcome the computational time problem and achieve relatively smooth switching angles in the area of operation [23], two global minimums where determined for a single operating point as described above. One in the area between $0 < \theta_U < \pi$ and one in the area of $\pi < \theta_U < 2\pi$.

From the first starting point an optimization with new constraints was executed into the direction of point $\theta_U = 0$ and $\theta_U = \pi$. The new constraint is that the new optimized alphas for the next operating point are allowed to vary by a maximum of ± 0.02618. If this condition is violated or there is no minimum within this area, a new starting point must be chosen for a second try. This new starting point is found by adding a random number between -0.04363 and 0.04363 to the initial starting point. This routine was repeated until a minimum was found that fulfills the constraints. Once the algorithm finds a minimum that fulfills the new constraints, these angles become the new initial values for the next iteration towards the boundaries. In this thesis a new optimization was executed for a constant ω_m, λ, m and every 0.03491 for θ_U .

For the area $\pi < \theta_U < 2\pi$ the procedure is the same, but with the initial angle values from the global minimum in this area.

To gain a controllable current control loop within a reasonable calculating time means not using the full potential of OPP.

Chapter 7

Results

In this chapter the results of the $I_{c,RMS}$ optimization at different operating points are illustrated and compared to the optimization executed in [2], where the optimization criterion was a low THD factor in the output current.
Due to the fact that equation (5.13) has a strong dependence on the motor rational speed, this variable additionally defines an operating point. For the further discussion an operating point is defined by an anisotropy factor λ, modulation index m, load voltage phase θ_U and mechanical rotational speed n_m. The anisotropy factor is set constant to 3.2 for this thesis.
In a further step, the resulting angles for an optimized $I_{c,RMS}$ in the operating point where $\theta_U = 3.8048$, $n_m = 9000rpm$, $\lambda = 3.2$ and $m = 0.6$, are fed to a Simulink/PLECS simulation. This simulation operated in this given operating point validates the correctness of equation (5.13), (5.10), (4.20) and the optimization itself.

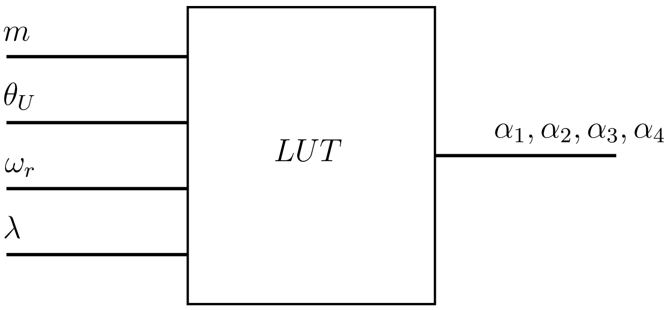

Figure 7.1: *Look-up table to gain the optimized switching angles during operation with the four input parameters, which define an operating point.*

7.1 $I_{c,RMS}$ Optimization at $n_m = 9000rpm$, $\lambda = 3.2$ and $m = 0.6$

Figure 7.2 represents the resulting angles of the $I_{c,RMS}$ optimization, which can be stored in a look-up table(see figure 7.1), in order to be able to access these angles during operation. The pre-optimization was executed at 1.0123 and 3.8048. From these points the optimization algorithm searched it‘s path to the boundaries 0 and

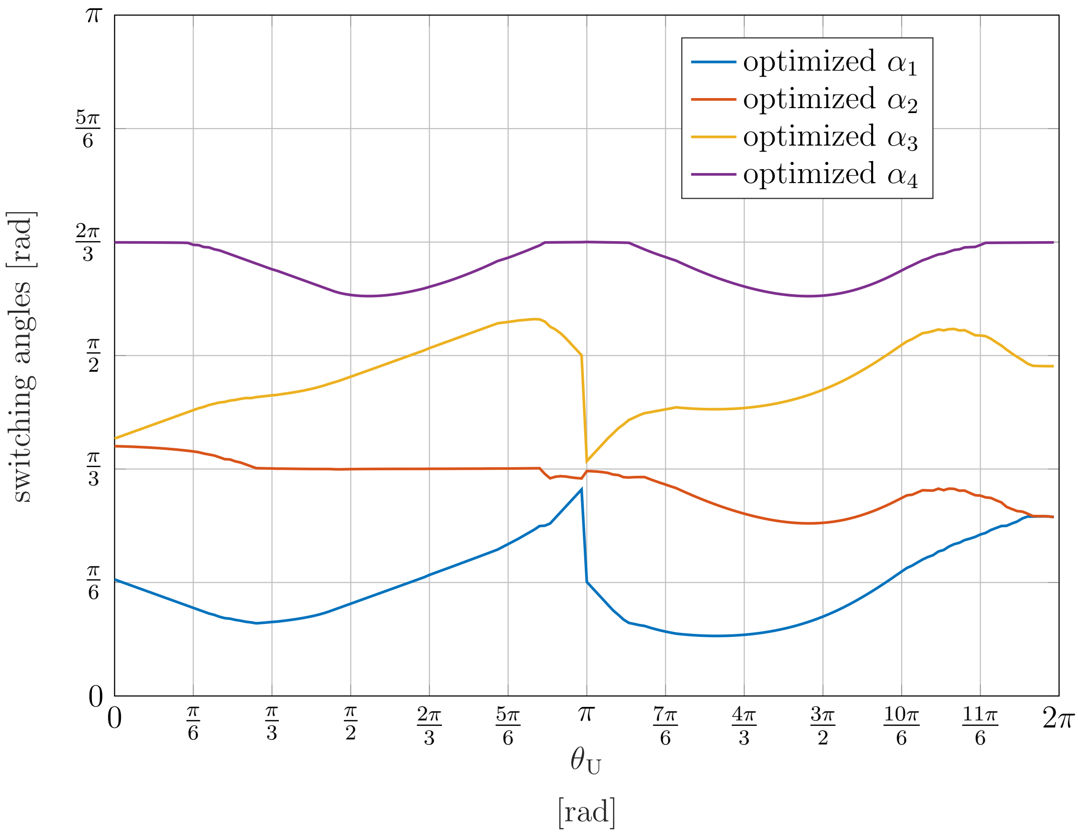

Figure 7.2: *Optimized angles for minimal* $I_{c,RMS}$ *at* $n_m = 9000rpm$ *and a modulation index of* 0.6.

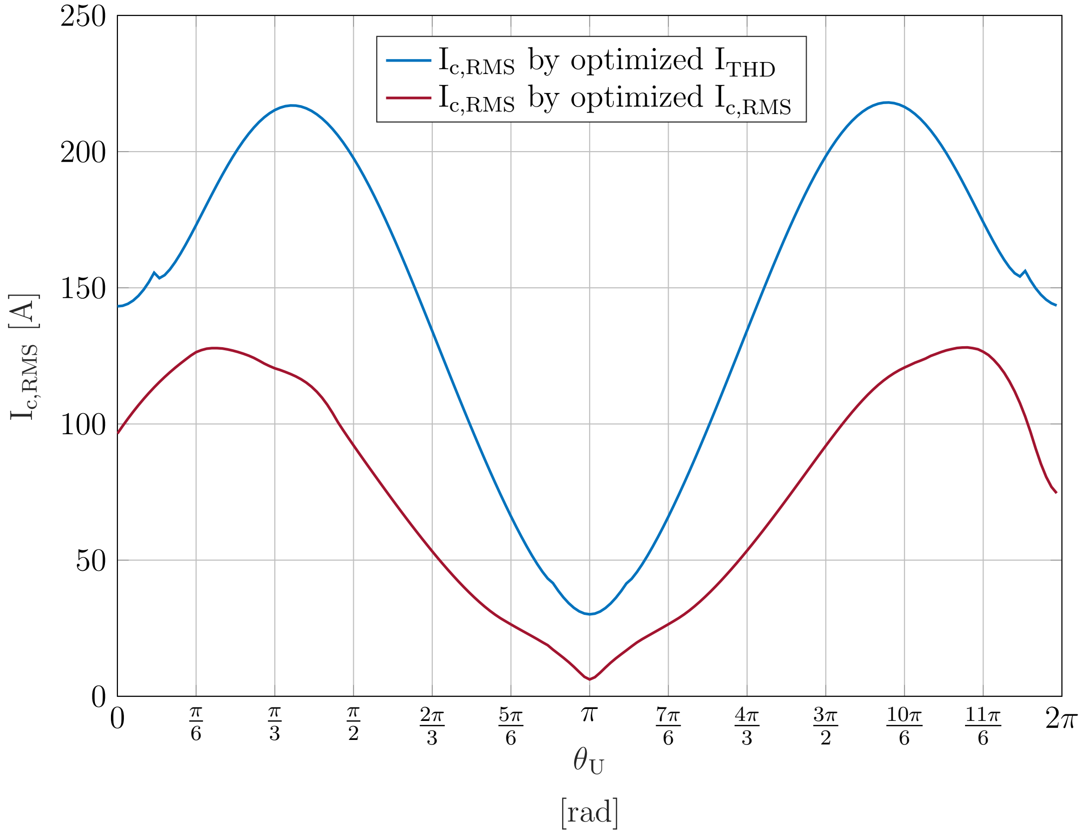

Figure 7.3: *$I_{c,RMS}$ for different optimization criteria at $n_m = 9000rpm$ and a modulation index of* 0.6*.*

3.1067 respectively π and 6.2483 with the constraint of a maximal deviation of ± 0.02618 from the previous angle.

Figure 7.3 illustrates the main message of this thesis. By applying the new OPP, where the optimization criterion was a minimal RMS current in the DC capacitor, the current $I_{c,RMS}$ can be reduced significantly for the whole range of θ_U demonstrated with the red line. The blue line shows the resulting $I_{c,RMS}$ by using the old OPP from [2], where the optimization criterion was a minimal THD in the output current.

Figure 7.4 shows the expected disadvantage of the new found OPP. By focusing on minimizing $I_{c,RMS}$ the THD factor for the output current increases. The red line represents the so resulting TDH current for the whole θ_U range.

Figure 7.5 is a enlarged sector from the figure 7.7 and displays the validation of the derived equation for the inverter current for the operating point $\theta_U = 3.8048$, $n_m = 9000rpm$, $m = 0.6$ and $\lambda = 3.2$. The green line represents the reference signal produced by a Simulink/PLECS simulation where the machine, battery, control-system and the VSI are modelled. The graph was recorded after 2 seconds where the machine was able to come in a steady operating point, while controlled in open loop. The red line represents the calculated inverter current by using equation (4.20) while the DC-link voltage is extracted from the simulation and fed into the calculation. This results in a very good approximation of the real inverter current. For the

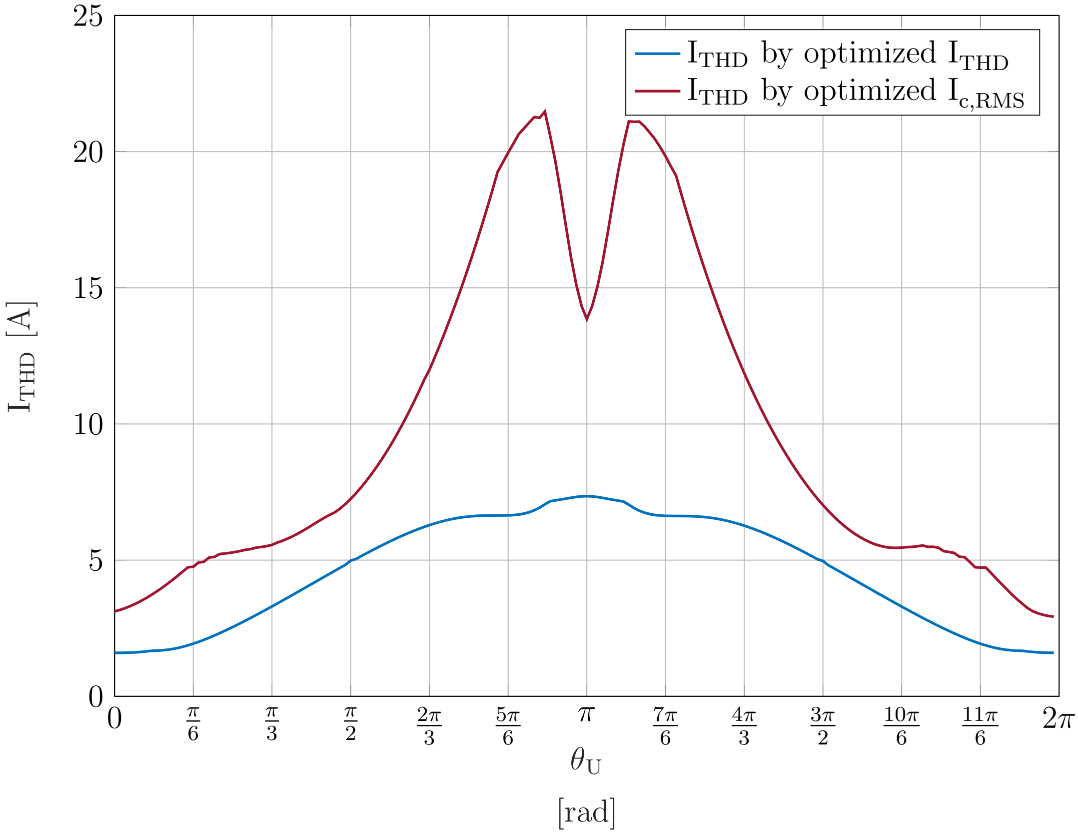

Figure 7.4: I_{THD} *for different optimization criteria at* $n_m = 9000rpm$ *and a modulation index of* 0.6.

calculation 100 harmonics have been considered. During optimization the variable U_{DC} is not known and therefore set to a constant value of $U_{DC} = 400V$. The so resulting calculated inverter current suffers in accuracy due to the simplification, seen as brown line in the figure.
Figure 7.6 was recorded during the same conditions as figure 7.5 and represents the current into the DC-capacitor. It illustrates also the problems of the Fourier approximation. Sharp peaks can not be represented well. This problem does not lead to a deviation in the RMS-current calculation. The $I_{c,RMS}$ is 32.31A over an electrical period for the reference signal. Inserting a variable U_{DC} into the equation (5.13) delivers for $I_{c,RMS} = 32.21$A. This small deviation can be neglected and is caused by the ignored stator resistor of the machine. Inserting a constant U_{DC} into the equation (5.13) delivers for $I_{c,RMS}$ 32.89A. The deviation due to the simplification is rather small (1.8 %). In other operating points the maximum deviation was as well approximately 1-3 %.
It should be noted that the harmonics which occur in the DC link are almost completely swallowed up by the DC link capacitor and thus hardly any harmonic currents have to be provided by the battery itself. This can be seen in figure 7.7 and 7.8, where the i_c graph looks very similar to the i_{inv} graph just without the DC offset.

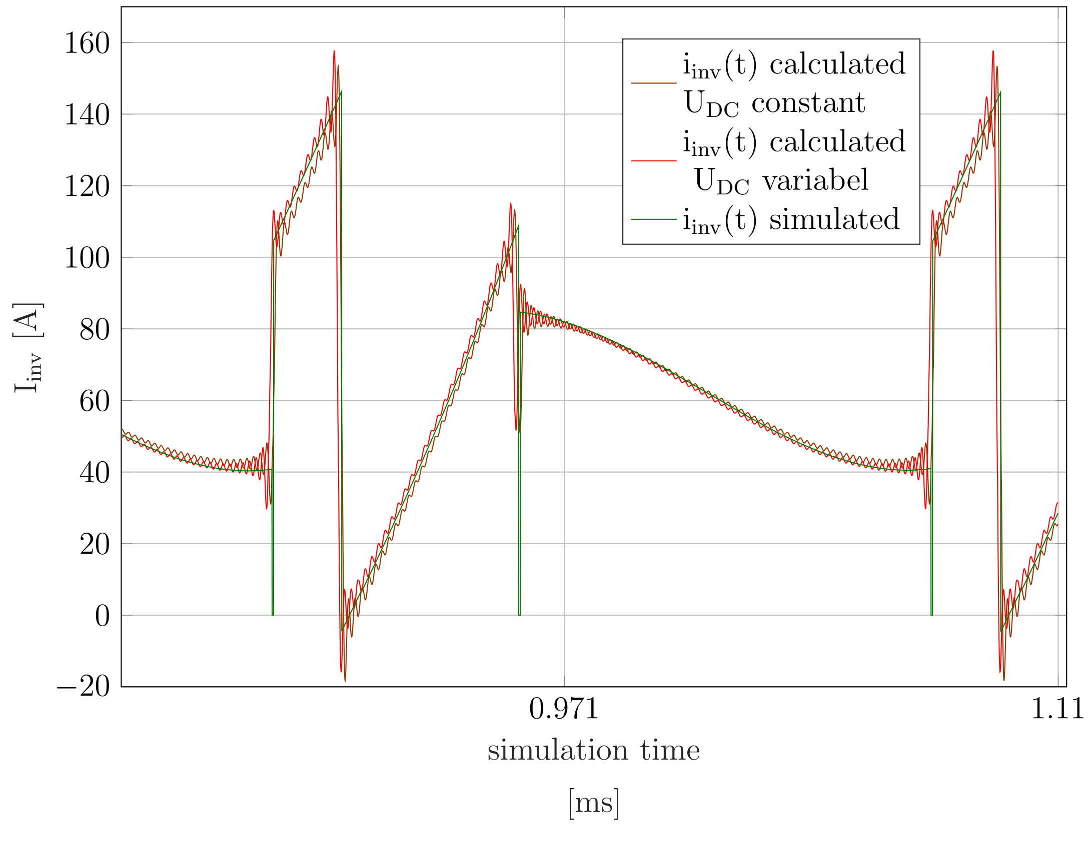

Figure 7.5: *Enlarged section of trace i_{inv} at $n_m = 9000rpm$ and a modulation index of* 0.6 *where θ_U is 3.8048.*

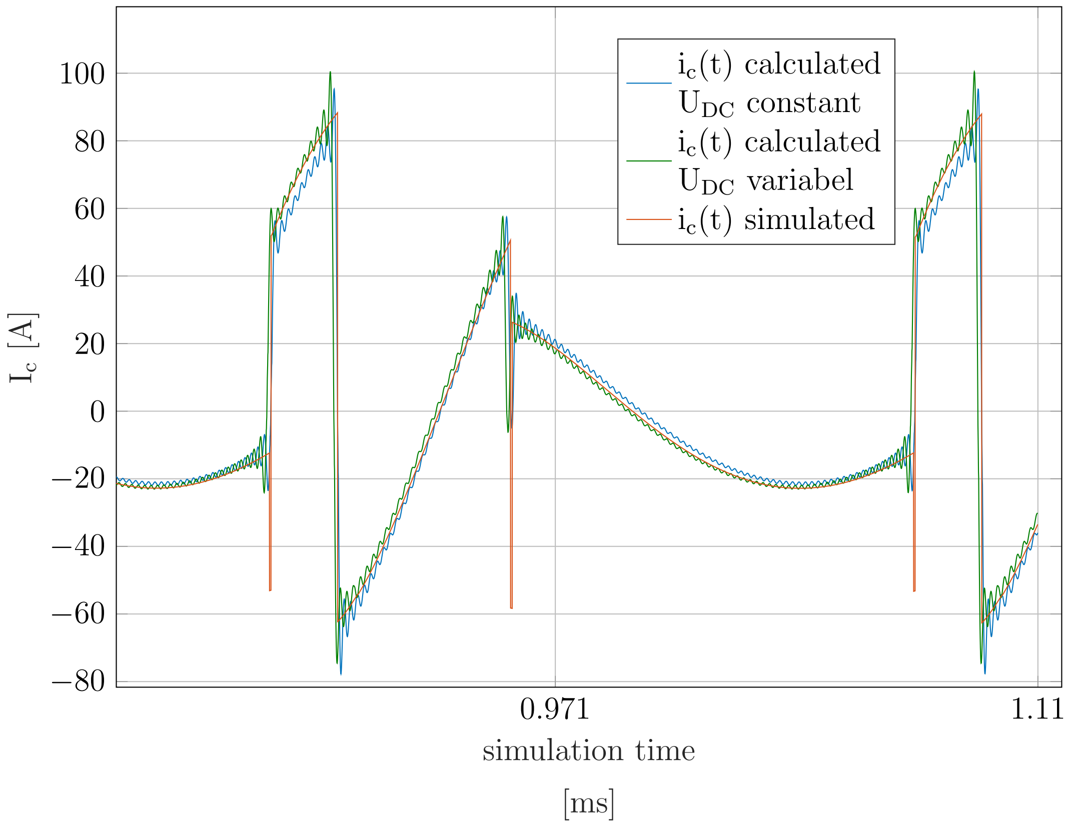

Figure 7.6: *Enlarged section of trace i_c at $n_m = 9000rpm$ and a modulation index of* 0.6 *where θ_U is 3.8048.*

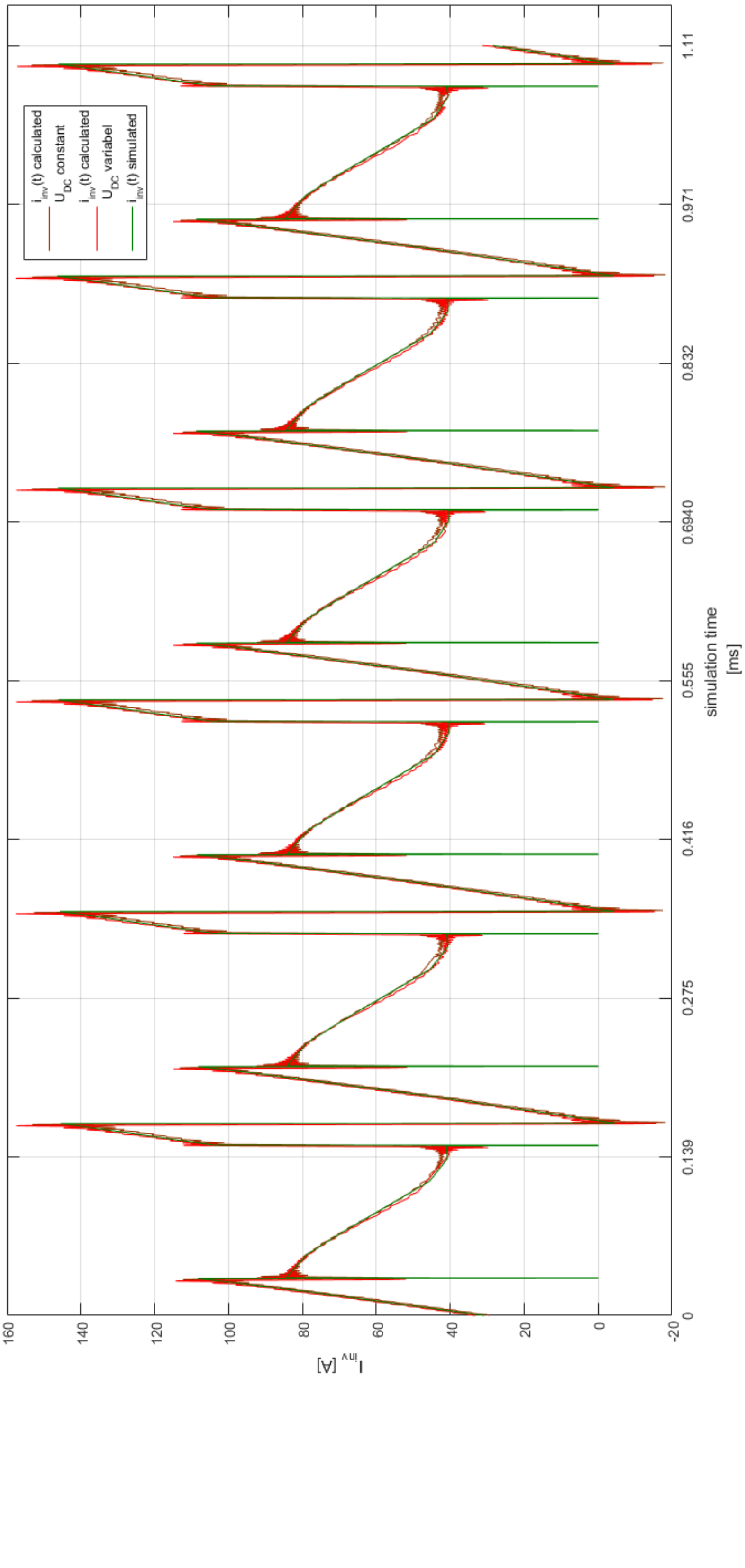

Figure 7.7: *Calculated and simulated i_{inv} recorded over an electrical period at $n_m = 9000rpm$ and a modulation index of 0.6 where θ_U is 3.8048.*

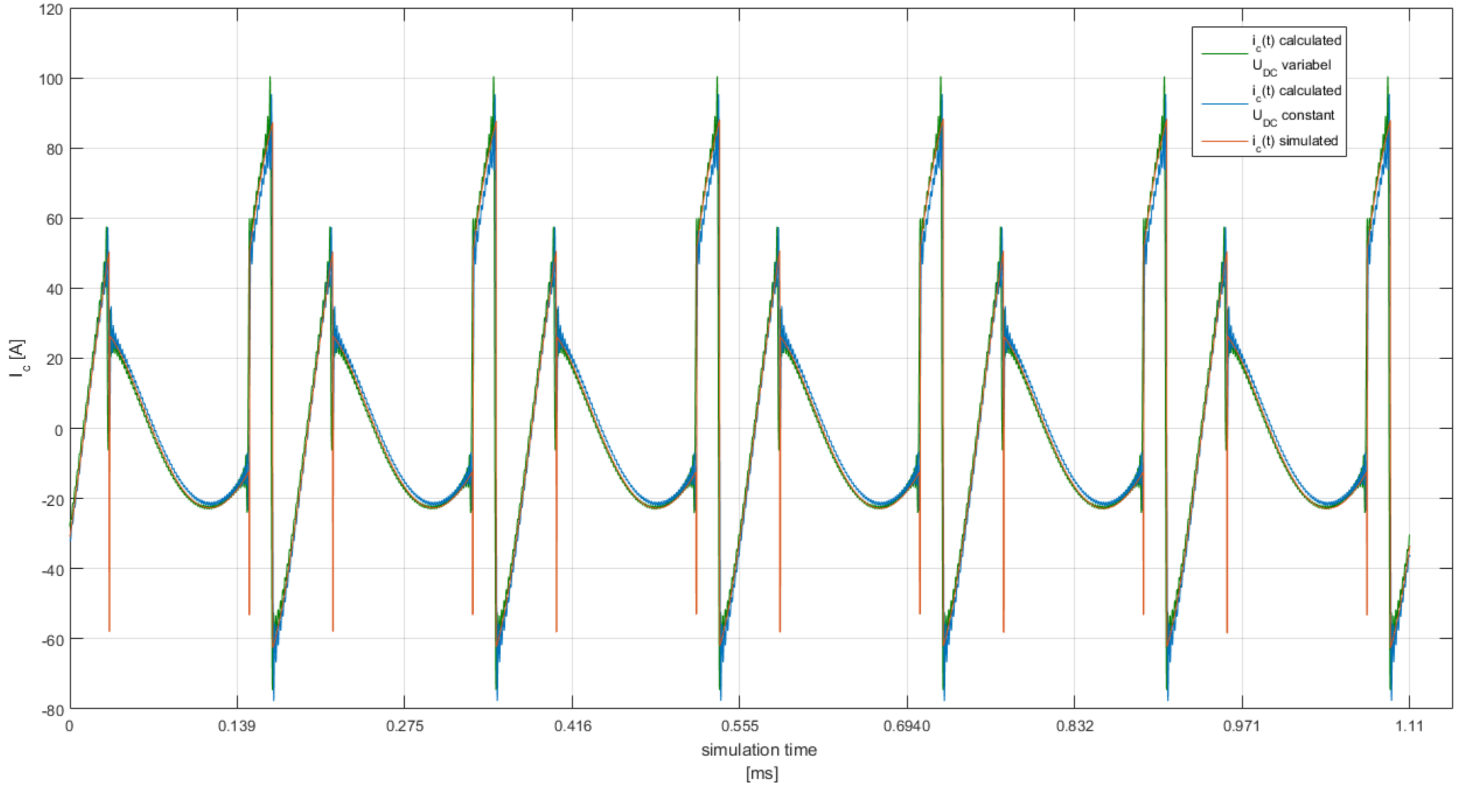

Figure 7.8: *Calculated and simulated i_c recorded over an electrical period at $n_m = 9000rpm$ and a modulation index of 0.6 where θ_U is 3.8048.*

7.2 $I_{c,RMS}$ Optimization at $n_m = 5000rpm$, $\lambda = 3.2$ and $m = 0.6$

Figure 7.9 displays the switching angles for a minimal RMS DC-link current at the given operating point. The pre-optimization was executed at $\theta_U = 1.5010$ and $\theta_U = 4.887$. The most important fact here to see is the mentioned strong dependency of equation (5.13) on the mechanical rotational speed of the motor. The resulting optimal angles are totally different at different speeds.
Figure 7.10 shows the resulting minimal $I_{c,RMS}$ for the calculated angles (red), the

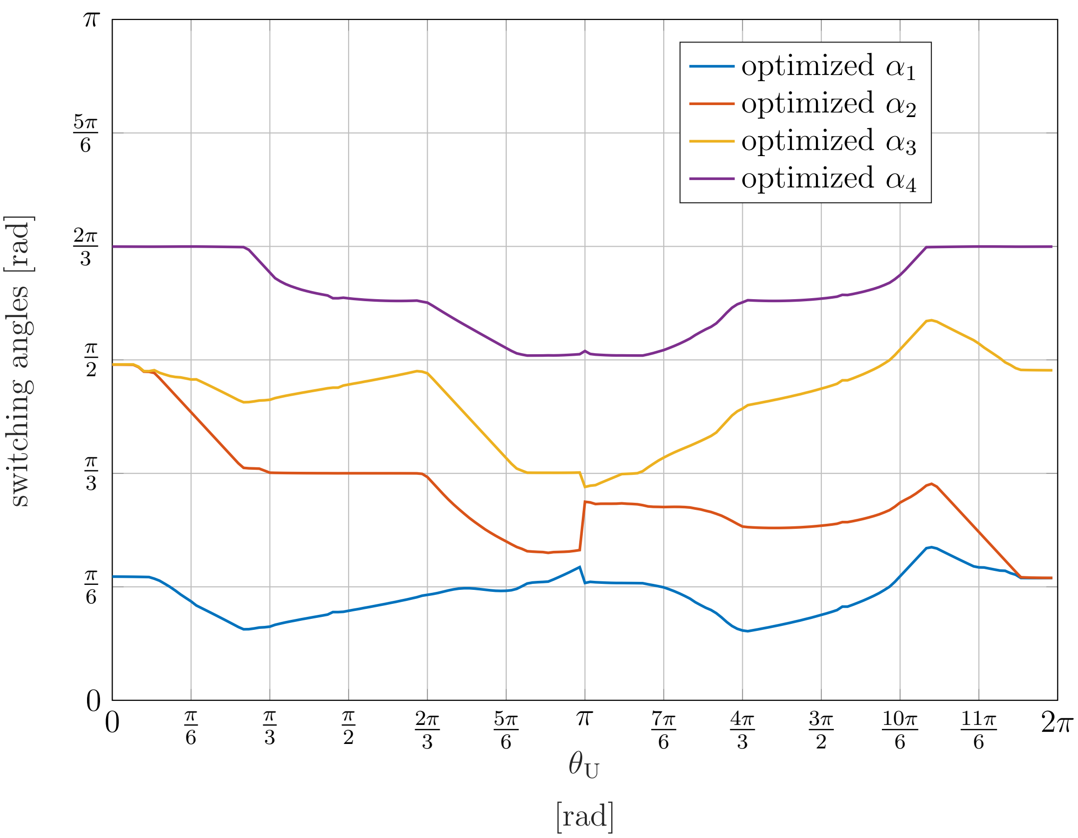

Figure 7.9: *Optimized angles for minimal $I_{c,RMS}$ at $n_m = 5000rpm$ and a modulation index of* 0.6.

$I_{c,RMS}$ graph for an optimized THD in the output currents (blue) from [2] and the the $I_{c,RMS}$ with the angles from the optimization at the operating point $n_m = 9000rpm$, $\lambda = 3.2$ and $m = 0.6$ (green dashed).
Figure 7.11 represents the graphs for the I_{THD} where the optimized angles for different optimization criteria and different operating points are used.

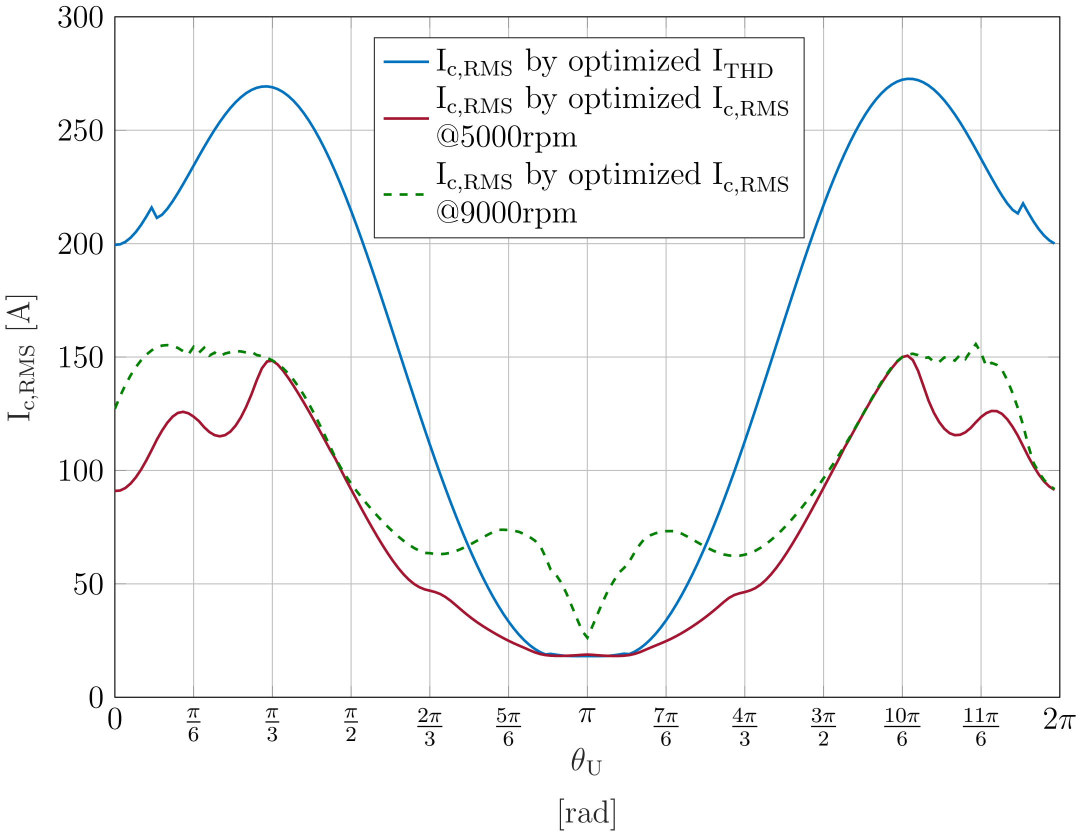

Figure 7.10: *$I_{c,RMS}$ for different optimization criteria at $n_m = 5000rpm$ as well as $n_m = 9000rpm$ and a modulation index of 0.6.*

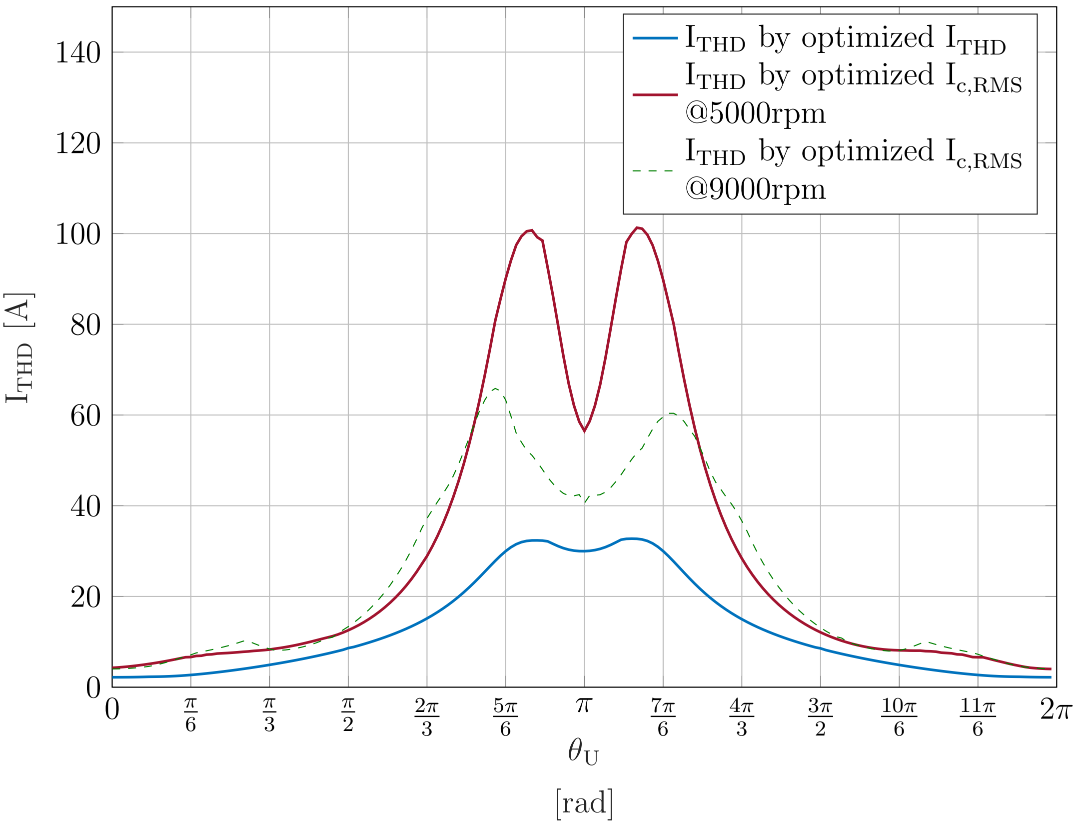

Figure 7.11: *I_{THD} for different optimization criteria at $n_m = 5000rpm$ as well as $n_m = 9000rpm$ and a modulation index of 0.6.*

7.3 $I_{c,RMS}$ Optimization at $n_m = 9000rpm$, $\lambda = 3.2$ and $m = 1.2$

Figure 7.12 illustrates the switching angles for a minimal RMS DC-current at the given operating point. The pre-optimization was executed at $\theta_U = 1.7104$ and $\theta_U = 4.5029$. For higher modulation indexes the figure 7.13 and figure 7.14 display

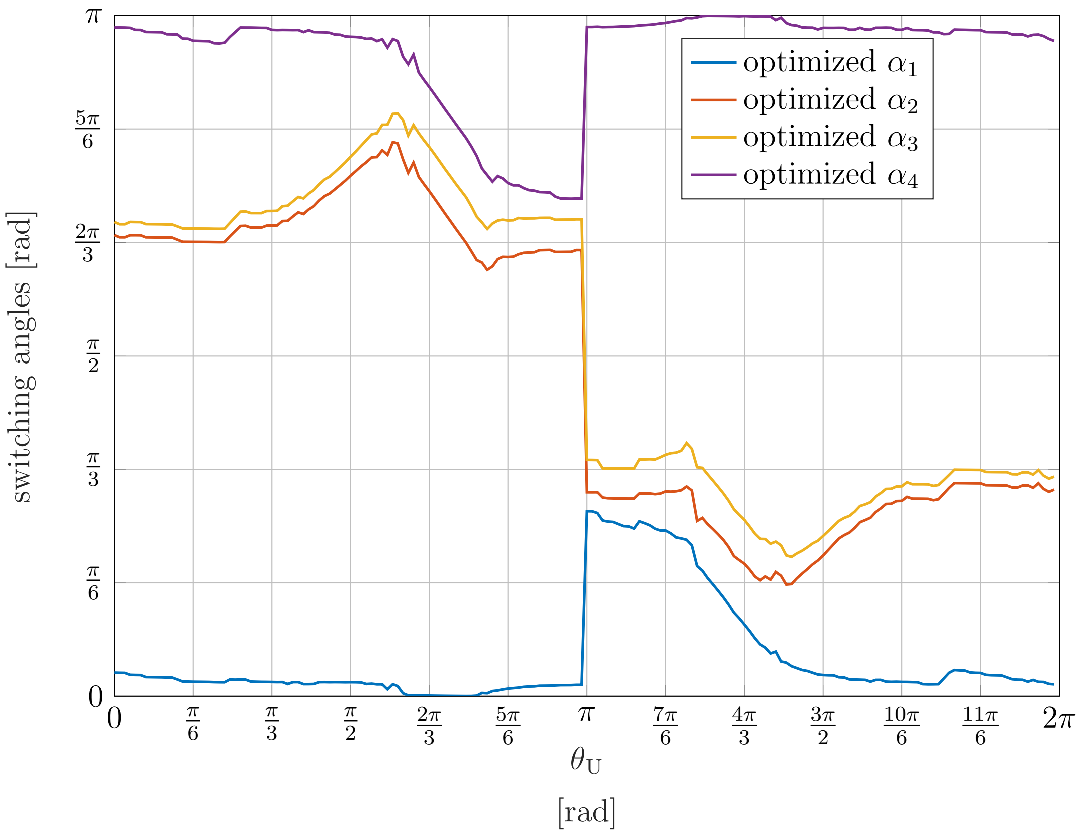

Figure 7.12: *Optimized angles for minimal $I_{c,RMS}$ at $n_m = 9000rpm$ and a modulation index of 1.2.*

the resulting $I_{c,RMS}$ and I_{THD}, respectively which occur while feeding the machine with two different optimized angles. The blue line represents an optimization for a low THD factor in the current output signal and the red line is designed to fulfill a minimal RMS current in the DC-link of the VSI. For high modulation indexes the difference between the two lines is not as big as for lower modulation indexes but still, an optimization which reduces the RMS current in the DC-link is possible.

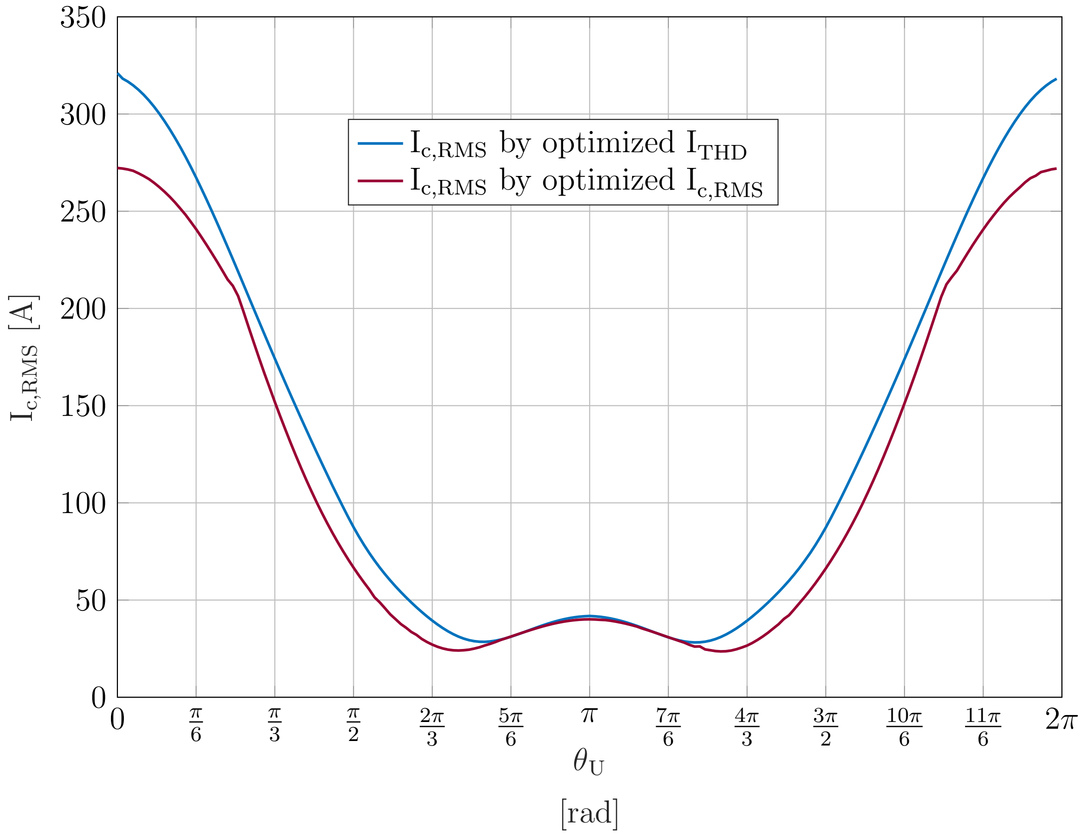

Figure 7.13: *$I_{c,RMS}$ for different optimization criteria at $n_m = 9000rpm$ and a modulation index of 1.2.*

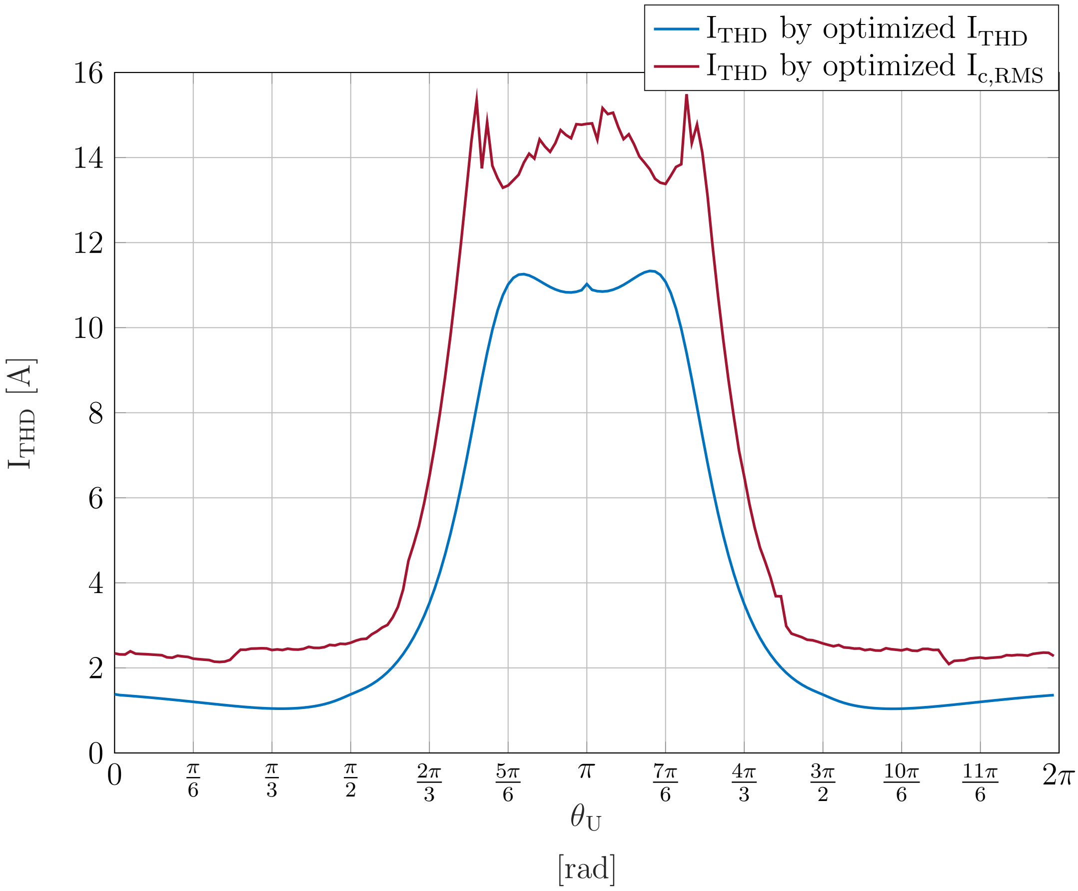

Figure 7.14: *I_{THD} for different optimization criteria at $n_m = 9000rpm$ and a modulation index of 1.2.*

Chapter 8

Conclusion

The presented thesis demonstrates a way of minimizing the RMS current in the DC-link of a two-level VSI by using optimized pulse patterns. Furthermore, an analytic equation for the inverter current and the capacitor current are derived in dependence on the switching angles of the power inverter. For the motor phase current (i_s^u, i_s^v, i_s^w) calculation the DC-link voltage was set constant. A further simplification with hardly any impact is the neglected stator resistor of the PMSM.
The derived equations for $I_{c,RMS}$, $i_c(t)$ and $i_{inv}(t)$ have a strong dependency on the rotational angular motor speed. Considering this dependency an operating point is defined by the combination of a motor rotational speed n_m, anisotropy factor λ, modulation index m and load voltage phase θ_U. The optimization process has to be repeated for each operating point and the resulting optimized switching angles are stored in look-up tables, in order to be able to use these angles during operation. Finally, for different operating points the correctness of the derived equations and the optimization algorithm itself are demonstrated with simulations in Simulink/PLECS.

Chapter 9

Outlook

In a future work the variable DC-link voltage should be considered for the motor phase current calculation to achieve a higher accuracy. If possible, it would be of great interest to eliminate the ω_m dependency in the derived equations for $I_{c,RMS}$, $i_c(t)$ and $i_{inv}(t)$. In this case the look-up tables can be reduced enormously and the optimization procedure gets simplified as well.
Most important to mention is the improvement potential in the optimization procedure itself. Due to the lack of calculating power only two **global** minima areas were searched in the whole θ_U range for each operating point where m, λ and ω_m were constant. And those with a relative rough step size of 0.1745 for the switching angles. In a future work this step size can be reduced to locate the **global** minima of an operational point more accurate. Additionally the optimization algorithm, which searches the other **local** minima for the whole θ_U range can be improved.

Bibliography

[1] J. Holtz. Pulsewidth modulation-a survey. *IEEE Transactions on Industrial Electronics*, 39(5):410–420, Oct 1992. doi:10.1109/41.161472.

[2] A. D. Birda, J. Reuss, and C. Hackl. Synchronous optimal pulse-width modulation with differently modulated waveform symmetry properties for feeding synchronous motor with high magnetic anisotropy. In *2017 19th European Conference on Power Electronics and Applications (EPE'17 ECCE Europe)*, pages P.1–P.10, Sept 2017. doi:10.23919/EPE17ECCEEurope.2017.8098963.

[3] A. K. Rathore, J. Holtz, and T. Boller. Synchronous optimal pulsewidth modulation for low-switching-frequency control of medium-voltage multilevel inverters. *IEEE Transactions on Industrial Electronics*, 57(7):2374–2381, July 2010. doi:10.1109/TIE.2010.2047824.

[4] A. Tripathi and G. Narayanan. Optimal pulse width modulation of voltage-source inverter fed motor drives with relaxation of quarter wave symmetry condition. In *2014 IEEE International Conference on Electronics, Computing and Communication Technologies (CONECCT)*, pages 1–6, Jan 2014. doi:10.1109/CONECCT.2014.6740342.

[5] Z. Zhang, X. Ge, Z. Tian, X. Zhang, Q. Tang, and X. Feng. A pwm for minimum current harmonic distortion in metro traction pmsm with saliency ratio and load angle constrains. *IEEE Transactions on Power Electronics*, 33(5):4498–4511, May 2018. doi:10.1109/TPEL.2017.2723480.

[6] G. S. Buja and G. B. Indri. Optimal pulsewidth modulation for feeding ac motors. *IEEE Transactions on Industry Applications*, IA-13(1):38–44, Jan 1977. doi:10.1109/TIA.1977.4503359.

[7] A. Edpuganti and A. K. Rathore. A survey of low switching frequency modulation techniques for medium-voltage multilevel converters. *IEEE Transactions on Industry Applications*, 51(5):4212–4228, Sept 2015. doi:10.1109/TIA.2015.2437351.

[8] A. Tripathi and G. Narayanan. Evaluation and minimization of low-order harmonic torque in low-switching-frequency inverter fed induction motor drives. In *2014 IEEE International Conference on Power Electronics, Drives and Energy Systems (PEDES)*, pages 1–6, Dec 2014. doi:10.1109/PEDES.2014.7042081.

[9] F. C. Zach, R. Martinez, S. Keplinger, and A. Seiser. Dynamically optimal switching patterns for pwm inverter drives (for minimization of the torque and speed ripples). *IEEE Transactions on Industry Applications*, IA-21(4):975–986, July 1985. doi:10.1109/TIA.1985.349568.

[10] H. Bai, F. Wang, T. Wang, and D. Wang. A svpwm/shepwm combined modulation strategy of starting inverter for a high speed generator power system. In *2009 35th Annual Conference of IEEE Industrial Electronics*, pages 136–141, Nov 2009. doi:10.1109/IECON.2009.5414796.

[11] K. Sato, M. Yoshizawa, and T. Fukushima. Traction systems using power electronics for shinkansen high-speed electric multiple units. In *The 2010 International Power Electronics Conference - ECCE ASIA -*, pages 2859–2866, June 2010. doi:10.1109/IPEC.2010.5542320.

[12] K. S. Amitkumar and G. Narayanan. Simplified implementation of space vector pwm strategies for a three level inverter. In *2012 IEEE 7th International Conference on Industrial and Information Systems (ICIIS)*, pages 1–6, Aug 2012. doi:10.1109/ICIInfS.2012.6304816.

[13] G. Shiny and M. R. Baiju. A fractal based space vector pwm scheme for general n- level inverters. In *The 2010 International Power Electronics Conference - ECCE ASIA -*, pages 847–854, June 2010. doi:10.1109/IPEC.2010.5543330.

[14] P. R. Rakesh and G. Narayanan. Analysis of sine-triangle and zero-sequence injection modulation schemes for split-phase induction motor drive. *IET Power Electronics*, 9(2):344–355, 2016. doi:10.1049/iet-pel.2015.0066.

[15] F. Wang. Sine-triangle vs. space vector modulation for three-level pwm voltage source inverters. In *Conference Record of the 2000 IEEE Industry Applications Conference. Thirty-Fifth IAS Annual Meeting and World Conference on Industrial Applications of Electrical Energy (Cat. No.00CH37129)*, volume 4, pages 2482–2488 vol.4, Oct 2000. doi:10.1109/IAS.2000.883171.

[16] J. Klima. Closed-form analytical investigation of an induction motor drive fed from four-switch inverter in six-step operation mode. In *2005 International Conference on Power Electronics and Drives Systems*, volume 1, pages 84–89, Nov 2005. doi:10.1109/PEDS.2005.1619665.

[17] Peter F. Brosch. *Moderne Stromrichterantriebe*, volume 3. Vogel Fachbuch, 1998.

[18] V. Gaikwad, S. Mutha, R. Mundhe, O. Sapar, and T. Chinchole. Survey of pwm techniques for solar inverter. In *2016 International Conference on Global Trends in Signal Processing, Information Computing and Communication (ICGTSPICC)*, pages 501–504, Dec 2016. doi:10.1109/ICGTSPICC.2016.7955352.

[19] Yongxing Wang, Xuhui Wen, Feng Zhao, and Xinhua Guo. Selective harmonic elimination pwm technology applied in pmsms. In *2012 IEEE Vehicle Power*

and Propulsion Conference, pages 92–97, Oct 2012. doi:10.1109/VPPC.2012.6422564.

[20] I. Ouannes, P. Nickel, and K. Dostert. Cell-wise monitoring of lithium-ion batteries for automotive traction applications by using power line communication: battery modeling and channel characterization. In *18th IEEE International Symposium on Power Line Communications and Its Applications*, pages 24–29, March 2014. doi:10.1109/ISPLC.2014.6812322.

[21] Lothar Papula. *Mathematik für Ingenieure und Naturwissenschaftler Band 2*, volume 12. Vieweg+Teubner, 2009.

[22] M. Huber, W. Amrhein, S. Silber, M. Reisinger, G. Knecht, and G. Kastinger. Ripple current reduction of dc link electrolytic capacitors by switching pattern optimisation. In *2005 IEEE 36th Power Electronics Specialists Conference*, pages 1875–1880, June 2005. doi:10.1109/PESC.2005.1581887.

[23] G. S. K, A. K. Rathore, A. Edpuganti, and D. Srinivasan. Optimal low switching frequency pulse width modulation of current-fed three-level inverter for solar integration. In *2016 IEEE Applied Power Electronics Conference and Exposition (APEC)*, pages 402–409, March 2016. doi:10.1109/APEC.2016.7467904.